Combining Near-Field and Far-Field Microscopy:

A new method for nanoscale super-resolution imaging

Master's thesis
University of Turku
Dept. of Physics and Astronomy
Physics
2011
BSc Kari Vienola
Supervisors:
MSc Tuomas Näreoja
PhD Jarno Salonen

TURUN YLIOPISTO
Fysiikan ja tähtitieteen laitos

VIENOLA, KARI: Lähikenttä- ja kaukokenttämikroskopian yhdistäminen: Uusi korkearesoluutioinen menetelmä nanokuvantamiseen.

Pro gradu -tutkielma, 71 s., 4 liites.
Fysiikka
Elokuu 2011

Osteoporoosi on sairaus, jossa luun uudistumisprosessi ei ole enää tasapainossa. Uuden luun muodostuminen on hitaampaa johtuen osteoblastien laskeneesta aktiivisuudesta. Yksi keino estää osteoporoosin syntyä on estää osteoklastien sitoutuminen luun pinnalle, jolloin ne eivät aloita luun syömisprosessia. Tämän Pro gradu -tutkielman tarkoituksena on luoda uusi työkalu osteoklastien sitoutumisen tutkimiseen samanaikaisesti fluoresenssi- ja atomivoimamikroskoopilla. Tätä tarkoitusta varten yhdistettiin atomivoimamikroskooppi sekä STED mikroskooppi. Kirjallisuuskatsauksessa käydään läpi yksityiskohtaisesti molempien mikroskooppitekniikoiden teoriat. Kokeellisessa osiossa esitetään käytetyt metodit ja alustavat tulokset uudella systeemillä. Lisäksi keskustellaan lyhyesti kuvan analysoinnista ImageJ-ohjelmalla.

Konfokaalisen fluoresenssimikroskoopin ja atomivoimamikroskoopin yhdistelmä on keksitty jo aikaisemmin, mutta tavallisen konfokaalimikroskoopin erottelukyvyn raja on noin 200 nanometriä johtuen valon diffraktioluonteesta. Yksityiskohdat eivät erotu, jos ne ovat pienempiä kuin puolet käytettävästä aallonpituudesta. STED mikroskooppi mahdollistaa fluoresenssikuvien taltioimisen solunsisäisistä prosesseista 50 nanometrin lateraalisella erotuskyvyllä ja atomivoimamikroskooppi antaa topografista tietoa näytteestä nanometrien erotuskyvyllä. Biologisia näytteitä kuvannettaessa atomivoimamikroskoopin erotuskyky kuitenkin huononee ja yleensä saavutetaan 30-50 nanometrin erotuskyky. Kuvien kerrostaminen vaatii vertauspisteitä ja tätä varten käytettiin atomivoimamikroskoopin kärjen tunnistamista ja referenssipartikkeleita. Kuva-analysointi suoritettiin ImageJ-kuvankäsittelyohjelmalla.

Tuloksista nähdään, että referenssipartikkelit ovat hyviä, mutta niiden sijoittaminen tarkasti tietylle kohdealueelle on hankalaa nanoskaalassa. Tästä johtuen kärjen havaitseminen fluoresenssikuvassa on parempi metodi. Atomivoimamikroskoopin kärki voidaan päällystää fluoresoivalla aineella, mutta tämä lisää kärjen aiheuttamaa konvoluutiota mittausdataan. Myös valon takaisinsirontaa kärjestä voidaan tutkia, jolloin konvoluutio ei lisäänny. Ensimmäisten kuvien kerrostamisessa käytettiin hyväksi fluoresoivalla aineella päällystettyä kärkeä ja lopputuloksessa oli vain 50 nanometrin yhteensopimattomuus fluoresenssi- ja topografiakuvan kanssa.

STED mikroskoopin avulla nähdään leimattujen proteiinien tarkat sijainnit tiettynä ajankohtana elävän solun sisällä. Samaan aikaan pystytään kuvantamaan solun fyysisiä muotoja tai mitata adheesiovoimia atomivoimamikroskoopilla. Lisäksi voidaan käyttää funktinalisoitua kärkeä, jolla voidaan laukaista signalointitapahtumia solun ja soluväliaineen välillä. Sitoutuminen soluväliaineeseen voidaan rekisteröidä samoin kuin adheesiomediaattorien sijainnit sitoutumisalueella. Nämä dynaamiset havainnot tuottavat uutta informaatiota solun signaloinnista, kun osteoklasti kiinnittyy luun pintaan. Tämä teknologia tarjoaa uuden näkökulman monimutkaisiin signalointiprosesseihin nanoskaalassa ja tulee ratkaisemaan lukemattoman määrän biologisia ongelmia.

Asiasanat: STED, fluoresenssi, osteoklasti, atomivoimamikroskooppi

UNIVERSITY OF TURKU
Department of Physics and Astronomy

VIENOLA, KARI: Combining Near-Field and Far-Field Microscopy: A new method for nanoscale super-resolution imaging

Master's thesis, 71 pp., 4 pp. app.
Physics
August 2011

Osteoporosis is a disease where bone remodeling process is not in homeostasis. Formation of new bone is slower due to decreased osteoblast activity. One way to prevent osteoporosis is to inhibit osteoclasts from binding to bone surface and start the resorption process. The purpose of this work is to create a tool to study osteoclast binding simultaneously with optical microscope and scanning probe microscope. To achieve this two imaging techniques, stimulated emission depletion (STED) microscope and atomic force microscope (AFM) were combined to produce a new imaging technique. In the literature review theories of both microscopy techniques are presented in detail. In the experimental section the methodology and preliminary results are presented. Additionally image analysis with ImageJ is briefly discussed.

A combination of confocal fluorescence microscope and atomic force microscope has already been invented but the resolution limit for optical microscope is approximately 200 nanometers due to diffraction limit of the light. Details that are smaller than half of the used wavelength cannot be resolved. STED microscope enables far-field fluorescence images from intracellular processes with a lateral resolution of 50 nanometers and AFM provides near-field topographical information in nanometer resolution in z-direction. With biological samples the lateral resolution of AFM is in the same range as the lateral resolution of STED microscope. To overlay the images, reference points are needed and for that tip position detection and reference particles were used. Image analysis was mainly done with image processing software ImageJ.

From the results it is clearly seen that reference particles are good but they should be precisely in the region of interest and this is difficult to achieve in nanometer scale. Therefore tip detection is more convenient method. The tip of the cantilever can be coated with fluorescent material although it increases the tip convolution. This can avoided by detecting autofluorescence or reflected (backscattered) light from the tip. The overlaying was done manually with 50 nanometer mismatch in the first images by using fluorescent tips.

STED microscope allows us to see the exact locations of labelled proteins at certain time inside a living cell. At the same time we can image the physical shape of the cell or measure adhesion forces with AFM. In addition, the functionalized AFM probes can be used to trigger signaling events between the cell and extracellular matrix (ECM). Binding to ECM can be recorded along with location of adhesion mediators in the binding domain. This dynamic observation produces further information on cell signaling during osteoclasts attachment. The new technology provides a nanoscale perspective to complicated signaling processes and resolves myriad of biological problems.

Keywords: Stimulated emission depletion, fluorescence, osteoclast, atomic force microscopy

Contents

Introduction

In this thesis two different imaging modalities were merged to produce a new method to image binding mechanisms of the osteoclasts to the bone surface: atomic force microscopy (AFM) and stimulated emission depletion (STED) microscopy. They were combined in order to gather new information about osteoclast binding to the bone surface.

Osteoclasts were discovered in 1873 by Kölliker [1]. They participate in calcium balance regulation and are responsible for the bone resorption in the bone remodelling cycle. These cells are large (40 µm diameter) and osteoclasts have multiple nuclei. AFM is commonly used in material and surface sciences since it provides a high resolution topographical map from the surface in atomic scale [2]. With AFM it is possible to use a method called force spectroscopy (FS) and it can be used to measure binding forces between the osteoclasts and the bone surface [3]. Where as AFM images the surface, STED is a super-resolution optical method based on normal confocal laser scanning microscope (CLSM). It uses a pinhole in front of the detector allowing the light only from the focal plane to pass through. The sample is scanned point-by-point with a laser using mirrors to move the laser in the sample. Three dimensional imaging is achieved when images from different depths are combined.

The stimulated emission depletion method manipulates the acquired fluorescence spot by switching off the major part of the fluorescence. This means that the diffraction limit of the light is no longer a limiting factor in the resolution of the fluorescence microscopy. In an optimized setup, resolution of 5.8 nanometres have been reported with extremely photostable nanodiamonds [4]. To conduct our experiments, a combination of STED and AFM had to be designed first. After this the image data was merged from both modalities. Information acquired from the images can be used to recognize different binders to develop blockers which will inhibit osteoclast binding

and eventually develop drugs for osteoporosis treatments.

1 Microscopy in science

The first microscope was invented in the late 16th century by Hans and Zacharias Janssen, although they did not release any publications about their invention [5]. Their microscope had two lenses and the magnification could be altered by changing the distance between the lenses. The magnification of this microscope was up to nine times. Since the invention of this first microscope, microscopy started to evolve rapidly.

Anton van Leeuwenhoek and Robert Hooke had a major impact on "popularizing" microscopy among the biologists. Hooke refined the compound microscope with a sample stage, an illuminator and focusing controls giving it the main components it has today (see fig. 1).

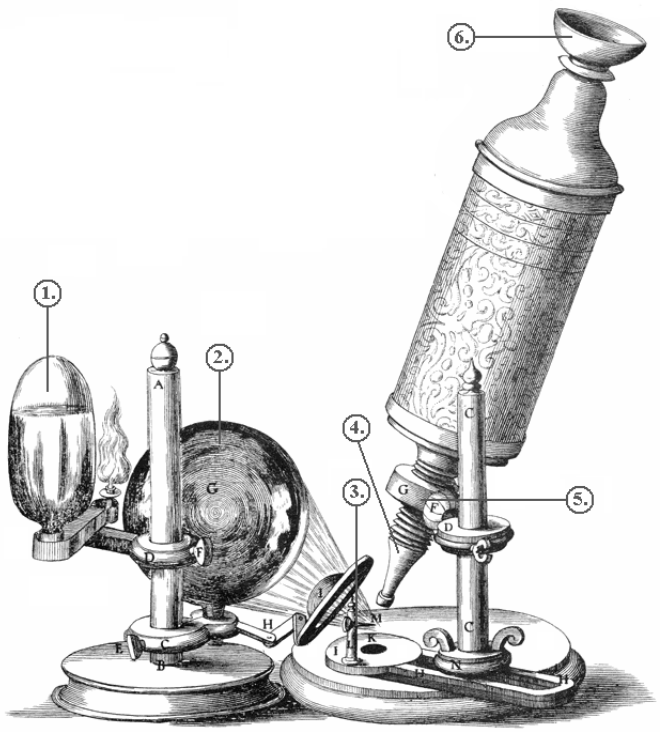

Figure 1. A drawing of Robert Hooke's microscope taken from his Micrographia. 1) Oil lamp for light source, 2) Round water flask to gather the light (condenser), 3) Specimen stage, 4) Objective, 5) Focusing screw and 6) Eyepiece [6].

He also published the famous "Micrographia" and was the first one to use word "cell". At the time it meant structure of cork [6]. The magnification of Hooke's microscopes varied from 30x-50x.

Around the same time Leeuwenhoek crafted his lenses carefully and invented a microscope which only had one lens but the magnification was 200x (see fig. 2). This magnification was good enough to see actual cells. He imaged red blood cells and spermatozoa and was later on accepted as a member of Royal Society [7] for his accomplishments. Leeuwenhoek's one lens microscope was superior compared to two lens systems in 1800th century because of the aberrations from the multiple lenses.

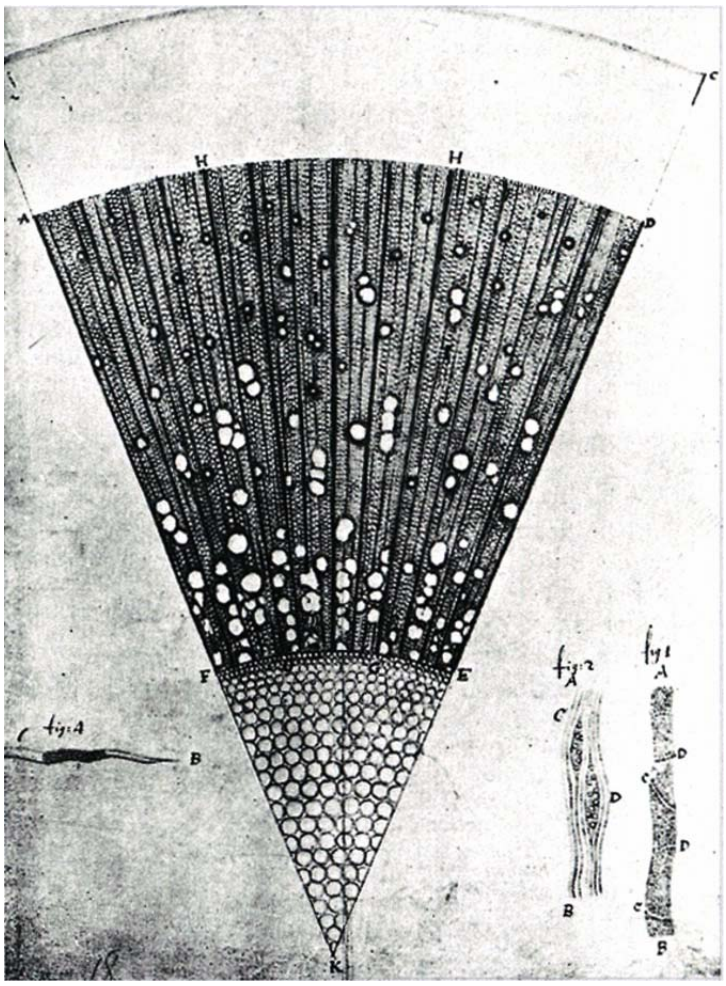

Figure 2. Microscopic section through one year old ash wood. The drawing is taken from one of Leeuwenhoek's letters [8].

With help of Otto Schott, Ernst Abbe developed lens that was chromatically and spherically corrected (apochromatic lens). Spherical correction reduced the blurriness in the edges and chromatic correction reduced the color distortion [9]. In 1874 Ernst Abbe published his well-known article titled: "A Contribution to the Theory of the Microscope and the nature of Microscopic Vision". In this paper Abbe explained the theoretical boundaries of modern light microscopy. Until the invention of STED microscope, this was thought to be a limit that can not be broken [10].

In 1893 Köhler illumination was invented by August Köhler [11]. This illumination produced an even illumination of the sample and ensured that the image of the illumination source was not shown in the result image. Light microscopy kept developing in the 20th century when phase contrast and differential interference contrast illumination were invented [12, 13].

In the middle of the 20th century electron microscope was invented [14, 15]. A superior resolution (500,000x magnification) compared to light microscopy was said to replace the light microscopy despite of its slow imaging rate and thin sample thickness compared to light microscopy. At the same time light microscopy went through changes when Minsky patented his confocal microscope in 1955 [5].

Scanning tunnelling microscope (STM) was invented in 1981 by Gerd Binnig and Heinrich Rohrer and they got the Nobel Prize in Physics for their efforts in 1986 [16]. This new imaging method scanned the surface and did not require any vacuum for imaging unlike scanning electron microscope (SEM) and the resolution was in atomic scale. Atomic force microscope (AFM) was invented a bit later in 1986 [17].

An alternative method for confocal microscope called two-photon microscopy was invented in 1990. This invention provided deeper sample depths and reduced phototoxicity [18]. Soon after this, 4Pi-microscopy was developed by Stefan Hell in 1991 [19, 20] followed by the invention of theta microscopy in 1994 [21]. Both

of these techniques improved lateral and axial resolution significantly in confocal microscopes. Next big step in microscopy was achieved in 1994 when Stefan Hell managed to demonstrate theoretically how to bypass the diffraction limit of the light [22]. In the 21st century, numerous applications were developed e.g. photoactivated localization microscopy (PALM) and stochastic optical reconstruction microscopy (STORM) [23, 24] and they all use different kind of methods to bypass the diffraction limit and general term for these methods is called point spread function engineering.

2 Atomic force microscopy

AFM is a part of scanning probe microscope family. It includes microscopy techniques which have a probe that interacts with a sample in some way to get a readable signal. In scanning near-field optical microscopy (SNOM) an optical detector is placed on the specimen surface distance between the probe and the sample being much closer than the applied wavelength, typically few nanometers [25]. Scanning tunnelling microscope (STM) uses the tunnelling effect which comes from quantum mechanics [16]. The tip is close to the sample so that the electrons can travel between the sample and the tip. Data is collected from the resulting current changes. In AFM data is collected with a probe that is scanning the surface either in contact mode or non-contact mode.

All of the above imaging modalities have probes which scan the sample area and produce different kind of images from the surface such as a topographical presentation of the surface or they can detect small forces such as 10-10^4 pN [26] with FS and this makes possible to study individual bonds, for example [27].

AFM is widely used in biological research. These include DNA and protein-DNA analysis [28], chromosome imaging [29] and the ligand-receptor binding [30]. It is also used in material sciences where scientists image the structure of the surface and breaking patterns [2]. Since there is an interaction between the tip and the

sample, FS is possible. This can be then used for studying how the viral infectious diseases work at the level of molecules or how the biomolecules assemble themselves [31]. Additionally, biological molecules can be attached to AFM probes. This will transform the tip into a biochemically selective sensor which can be used to record recognition maps and force spectra.

2.1 Properties of AFM

AFM was invented in 1986 by Calcin Quate and Christoph Gerber after the invention of STM. To image the area of interest, AFM is equipped with a cantilever which has a small tip and this tip interacts with the sample surface. Since the surface is not smooth, the cantilever reacts on height differences during the scanning. The basic illustration of a typical AFM is presented in the figure 3.

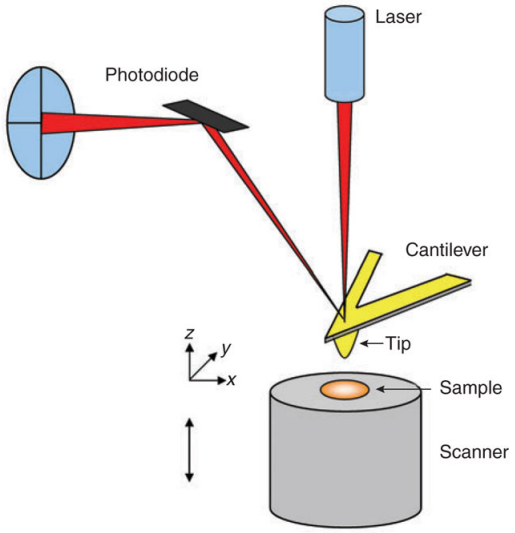

Figure 3. The basic setup of AFM. First the laser is focused to the cantilever. Light is then reflected to the photodiode and the cantilever bending is detected. In this setup the sample is moved with the scanner and the cantilever is staying still. Another option is that the sample stays still and the cantilever is moved with a piezoelectric scanner [32].

To acquire the position of the tip, a laser beam is focused on to the cantilever where it reflects to the quadrupole photodetector. The photodiode transforms cantilever deflection into a readable signal. This signal travels to a feedback unit.

The feedback loop is used for maintaining a constant force (the deflection is kept constant) between the sample and the tip in the contact mode or the amplitude in non-contact mode. Modern equipment can measure various properties from the sample (e.g. magnetic and electric properties) but specialized tips are required to do these kind of measurements [33, 34].

2.2 Piezoelectric scanner

Piezoelectric scanners are based on the piezoelectric effect. When a voltage is applied to the scanner (in this case a piezoelectric tube), a crystal will expand or contract. This deformation is proportional to the voltage applied [35]. All three dimensions are controlled with the piezoelectric scanner since it provides a superior precision. AFMs can use either a tube scanner or a sample scanner and they will move in x-, y- and z-directions. In comparison to tube and sample scanners, a flexure scanner completely decouples the X/Y-scanner motion from the Z-scanner movement. Scanners are more sensitive in the beginning of the scan and this sensitivity difference can be seen when comparing trace and retrace images. These scanners are stable and will seldom need recalibration.

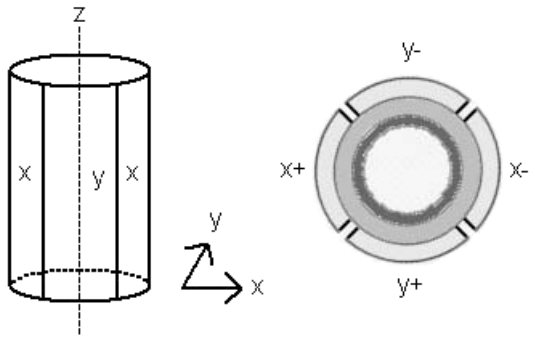

Figure 4. An illustration of a piezoelectric tube [36].

2.3 Factors contributing to resolution

In AFM the tip has a big effect in the resolution. By modifying the tip, the resolution can be enhanced significantly but it can make the tip more fragile. Modern tips can have a radius of less than 10 nm (can vary between 1-40 nm) and they are categorized for different purposes such as high resolution, general purpose and long scanning [37]. In the figure 5 there is a SEM image of a typical AFM cantilever and tip. The reason to modify the tip comes from tip convolution. The tip convolution

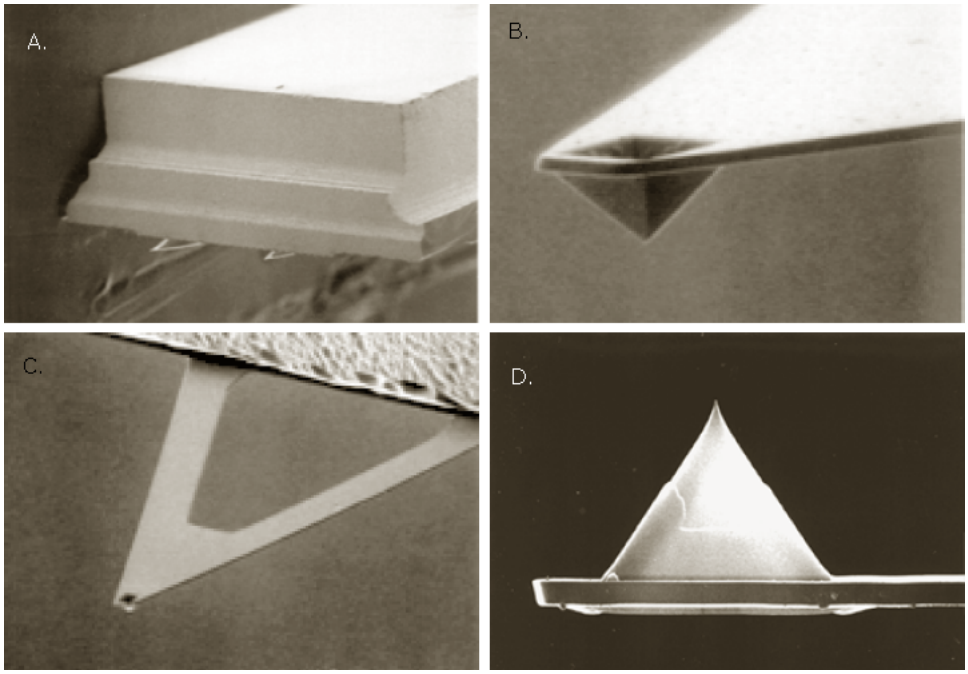

Figure 5. The cantilever and the tip imaged with SEM. In pictures A, B and C applied voltage was 5 kV and in D 20,000 kV. Picture A has a magnification of 65x, B has 5,000x, C has 800x and D has a magnification of 10,000x [38].

is illustrated in the figure 6. If the tip is sharper than the features in the sample, no artefacts are present. When a feature in the sample is sharper than the tip, the image will be dominated by the shape of the tip and the image is convolved as seen in figure 6B. Deconvolution is a mathematical method to decrease the artefacts that an instrument (in this case the tip of the AFM) causes to the image. In physical measurements the equation for the convolution is

$$(f * g) + \varepsilon = h, \tag{1}$$

where h is the recorded signal, f is the signal we want to recover, g is the signal that convolved the original signal and ε is white noise. The symbol $*$ signifies the convolution. To get the signal f, we need to know or estimate g in order to do the deconvolution and in AFM the tip causes convolution so information about the tip geometry is needed. When talking about resolution of images, also the pixel size

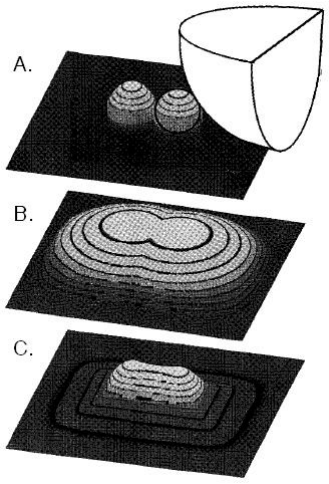

Figure 6. In A there is a sample surface with two objects and an ideally shaped spherical tip. B presents the image acquired from the two objects and the same picture is illustrated in C after the deconvolution [39]. The information about the tip geometry is required in order to do the deconvolution.

should be noticed. If the image size is 512 x 512 pixels and the scanning area is 1 µm × 1 µm, then the step size would be 1 µm ÷ 512 ≈ 2 nm. In z-axis you can either have 8-, 16- or 32-bit pixels. The amount of bits determines how many different shades of color you have in one pixel. In the 8-bit images there are $2^8 = 256$ different shades of grey starting from 0 (black in grey scale) and ending to 255 (white in grey scale). Resolution in z-axis is always better than the lateral resolution.

2.4 Intermolecular forces

Intermolecular forces are weak compared to intramolecular forces (e.g. covalent bond). These weak forces are particularly important in terms how molecules interact and form biological organisms.

2.4.1 Dipole-dipole and ion-dipole forces

It is known that molecules have uneven distribution of charge. Partial positive and partial negative regions exist in different regions of the molecule, forming a dipole. Dipole-dipole forces exist between neutral polar molecules. Polar covalent molecules act as little magnets; they have positive ends and negative ends which attract each other. In ion-dipole interaction ion and dipole are attracted to each other [40].

2.4.2 London dispersion forces

These forces are part of Van der Waals forces and they interact between atoms and molecules. The London dispersion force is caused by correlated movements of the electrons in interacting molecules. These forces exist because, at any given time, the electrons in an atom or a molecule are unevenly distributed. The uneven distribution of electrons creates an instantaneous dipole. The strength of these forces increases as the molecular weight increases [40].

2.4.3 Hydrogen bonding

Hydrogen bonding occurs between molecules that have a hydrogen atom bonded to a more electronegative atom, such as nitrogen, oxygen or fluorine. Hydrogen bonds (10-40 kJ/mol) are stronger than London and dipole-dipole forces (0.1-10 kJ/mol). Intermolecular hydrogen bonding is responsible for the high boiling point of water (100 ^{o}C) compared to the other group 16 hydrides that have no hydrogen bonds [40].

2.4.4 Induced dipole interaction

An ion-induced dipole attraction is a weak attraction that results when the approach of an ion induces a dipole in an atom or in a nonpolar molecule by disturbing the arrangement of electrons in the nonpolar species. A dipole-induced dipole attraction

is a weak attraction that results when a polar molecule induces a dipole in an atom or in a nonpolar molecule by disturbing the arrangement of electrons in the nonpolar species [40].

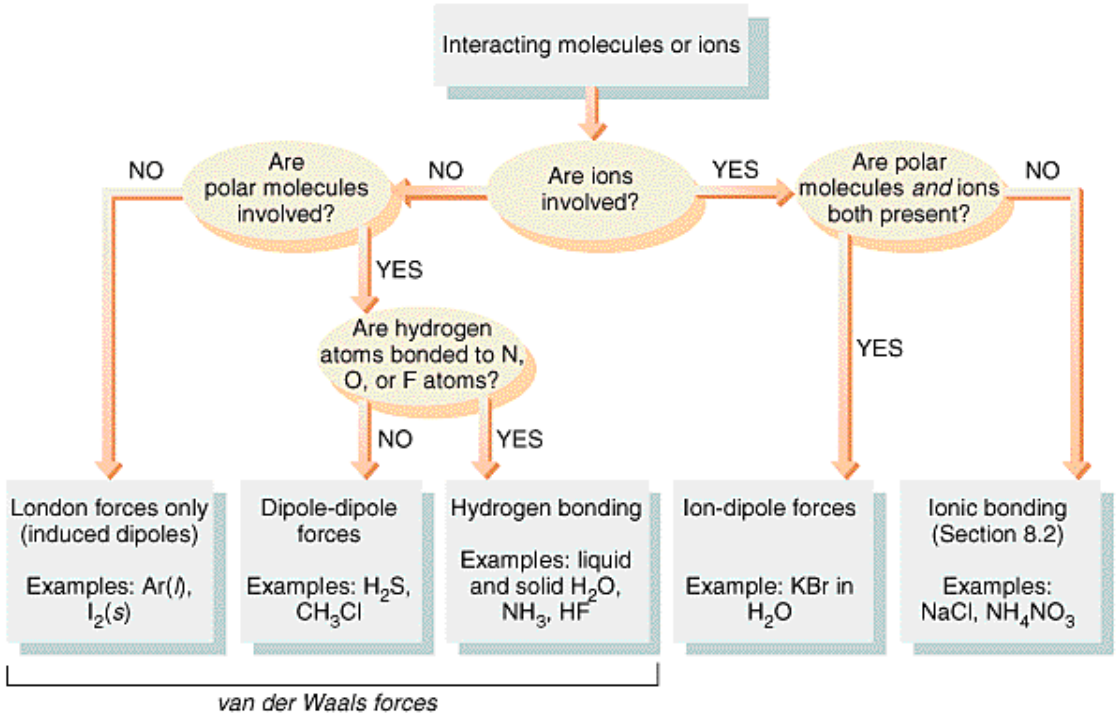

Figure 7. Summary of different intermolecular forces [41].

2.5 Scanning modes

2.5.1 Contact mode

The most popular imaging mode is the contact mode (also known as the static mode) where the tip is in a perpetual contact with the sample. The force between the tip and the sample is held constant. When the cantilever moves on the surface, deflection of the cantilever gives us signal either to raise or lower the sample or tip using the piezoelectric tube. Minimum force between the tip and the sample when the deflection is up can be calculated from

$$F_C^{min} = k \cdot z_{up} \tag{2}$$

where F_C is the force, k the spring constant (typically 0.001-5 nN/nm) and z is the deflection. In the figure 8 the force is plotted as a function of distance z.

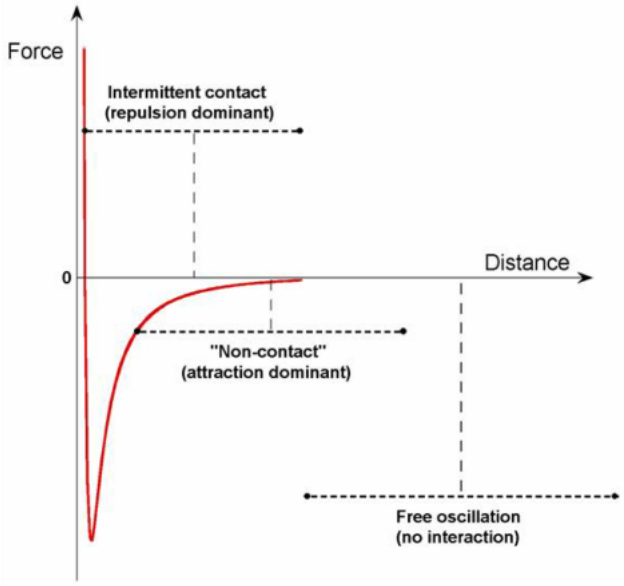

Figure 8. When using contact mode microscope is operating in the intermittent contact area of the curve and when working with the oscillation mode and e.g. FS, microscope is operating in the attractive regime of the force curve [42].

2.5.2 Non-contact mode

The oscillation mode (non-contact mode) was invented in 1987 shortly after AFM. In this mode the cantilever oscillates with a resonant frequency and do not touch the surface [43]. In non-contact mode AFM is working on the repulsive regime of the curve (see fig. 8). The feedback loop responses to the changes in the amplitude or the frequency by adjusting the distance between the tip and the sample and maintaining it constant. The software creates a topographical presentation of the surface from the changes in the cantilever's vibrations. This mode is normally used for soft samples although it can be used on hard samples as well. The tip and sample degradation is minimal since there is no contact. In tapping mode (intermittent contact mode) the cantilever is also oscillating. The amplitude is much higher, between 100-200 nm and the tip is tapping the sample. Stiffer cantilevers are used compared to the

contact mode and their spring constant is more than 20 N/m [44].

2.5.3 MAC mode

The magnetic AC (MAC) mode is used to obtain high resolution AFM images from delicate and soft samples e.g. living cells [45]. It was developed by Agilent Technologies Inc. [46, 47]. To use the MAC mode, the cantilever should be magnetically coated. It is then driven by an oscillating magnetic field and this gives precise control of the oscillation amplitude and excellent force regulation. Signal-to-noise-ratio is greatly increased in the MAC mode so the cantilever can be operated at much smaller amplitudes. Also the fluid imaging is improved due to the increased ratio. With the MAC-mode vertical or lateral modulation studies can be performed and plot a graph amplitude vs. frequency in contact. Spurious resonances, which can be seen in the fluid tapping mode, are also eliminated in MAC mode. The main difference between the non-contact mode and the MAC mode is the method for the tip oscillation. With non-contact mode the chip (where cantilever is attached) is oscillated with the piezoelectric transducer and the tip oscillates a bit differently than the chip. In MAC mode the tip is oscillated with a magnetic field and this gives us high precision compared to tapping and non-contact mode by reducing noise produced by chip resonance.

2.5.4 Force spectroscopy

FS measures the polarity and the strength of the interaction between the tip and the sample. This measured interaction between the tip and the sample is force in the attractive regime (see fig. 8). In FS the sample is not actually scanned and the cantilever works as a sensor (non-scanning configuration). To measure the force between the tip and the sample we can use Hooke's Law and get

$$F = k_c \cdot Z_c, \tag{3}$$

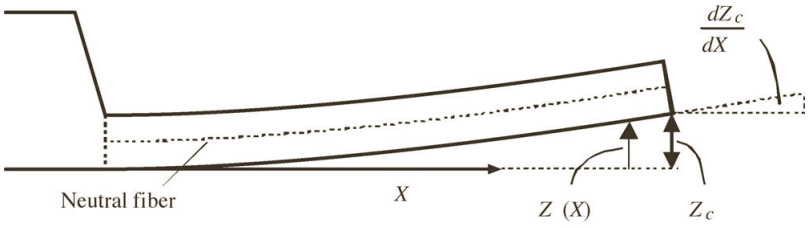

Figure 9. A schematic side view of a cantilever with a force at its end. X is the horizontal coordinate originating at the basis of the cantilever, $Z(X)$ is the cantilever deflection at the position X, Z_c being the cantilever deflection at its end [48].

where k_c is the spring constant and Z_c is the deflection of the cantilever. Z_c is detected with the position sensitive detectors when the laser is reflected from the cantilever. When the cantilever is affected by a force, it will bend and the reflected light beam moves through an angle equal to twice the change of the end-slope $\mathrm{d}Zc/\mathrm{d}X$. This is illustrated in figure 9.

For a cantilever with a rectangular cross-section of width w, length L and thickness t_c the equation for the change of the end-slope is

$$\frac{\mathrm{d}Z_c}{\mathrm{d}X} = \frac{6FL^2}{Ewt_c^3}, \tag{4}$$

where E is Young's modulus of the cantilever material, F is the applied force on the tip of the cantilever in normal direction. The detected signal is proportional to the end-slope of the cantilever. The deflection of the cantilever can then be expressed with an equation:

$$Z_c = \frac{4FL^3}{Ewt_c^3} = \frac{2}{3}L\frac{\mathrm{d}Z_c}{\mathrm{d}X}. \tag{5}$$

Equations 4 and 5 work only when system is in equilibrium. If the movement of the cantilever is significantly faster than allowed by its resonance frequency, these equations are not valid. The spring constant can be derived from the equation 3 and 5:

$$F = k_c \cdot Z_c \Rightarrow k_c = \frac{F}{Z_c} = \frac{Ewt_c^3}{4L^3}. \tag{6}$$

From the equation 6 is seen that a high sensitivity is achieved, when the spring constant is small or ratio t_c/L is low. In this equation the spring constant is defined

with dimensions and properties of the cantilever material. To have a good deflection, the cantilever should be long and thin.

Commercial AFM systems use different kind of method to calibrate the spring constant. This method was developed by Hutter and Bechhoefer and they suggested to measure the intensity of thermal noise [49]. In this method the spring constant gets the form

$$k_c = \beta^* \frac{k_B T}{\langle Z_1^{*2}(L) \rangle}, \tag{7}$$

where Z_1^* is the effective deflection of the first vibration mode and $\beta^* = 0,817$. The term $k_B T$ is the average energy of the vibration mode. More detailed mathematical derivations has been described in detail by Butt et al. [48].

When a cell attaches itself to a surface, another cell or extracellular matrix (ECM), it is called cell adhesion [50]. To measure these interactions, functionalized cantilevers are needed. A tipless cantilever is functionalized so that cell attaches to the cantilever. Then the cantilever is lowered to the surface (e.g. ECM) for a moment and pulled up [51]. The applied force to break the interactions between the cell and the surface is measured.

Molecules can be attached to a tip with polyethylene glycol (PEG) linkers. With this method single binding forces can be studied. The strength of the interaction between the molecule and its binding site is called affinity. These binding forces can be ionic bonds or Van der Waals forces, for example. High affinity means greater force in intermolecular interactions.

2.5.5 PicoTREC

A topography and recognition imaging system PicoTREC™ was developed by Molecular Imaging Corp., which is now part of Agilent Technologies. It combines real time detection of molecular recognition events and single molecule sensitivity. This system is used in a combination with MAC mode to provide a precise control.

Sensor molecules are attach to magnetically coated AFM tip with PEG tether. This way the sensor molecule can freely reorient itself to properly bind itself to its target on the surface. When recognition event occurs, several signals are detected. These include signals that correspond to the forces required to break hydrogen bonds and weaker short range interactions that are involved in specific molecular binding events [52].

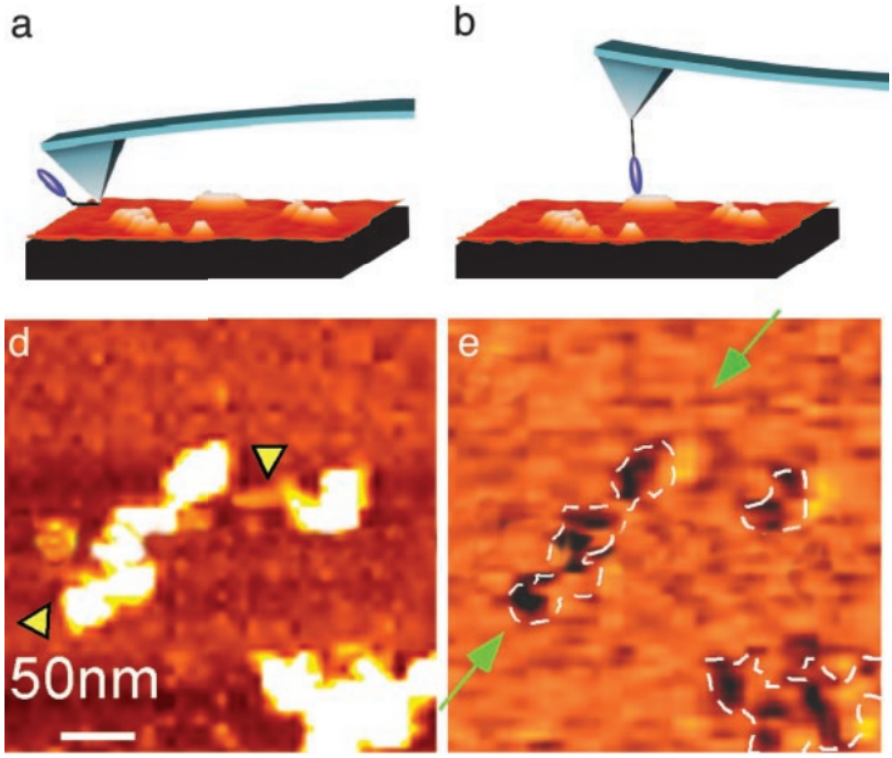

Figure 10. a) AFM tip with an antibody attached (blue blob) to the tip via PEG before binding to the target b) Scanning is started and antibody binds to an antigen. This binding can be seen as a reduction of the oscillation amplitude. PicoTREC acquires images *d* and *e* simultaneously. First one is the topographical presentation and the second one shows where binding occurred. Highest features in the topographical image are $\sim$ 5 nm. Adapted from the original picture [53].

Acquired signals are resolved and plotted separately. When using MAC mode with PicoTREC, maps of specific binding sites can be obtained. First image is the topography of the target molecules on the surface. Second image displays the specifically recognized target molecules on the surface (see fig. 10).

Molecular recognition is done by processing the reduction in oscillation ampli-

tude. When there is a binding, amplitude decreases. Imaging servo restores the original amplitude but it is shifted downwards. This peak shift provides the recognition signal for a specific antigen-antibody recognition event [53].

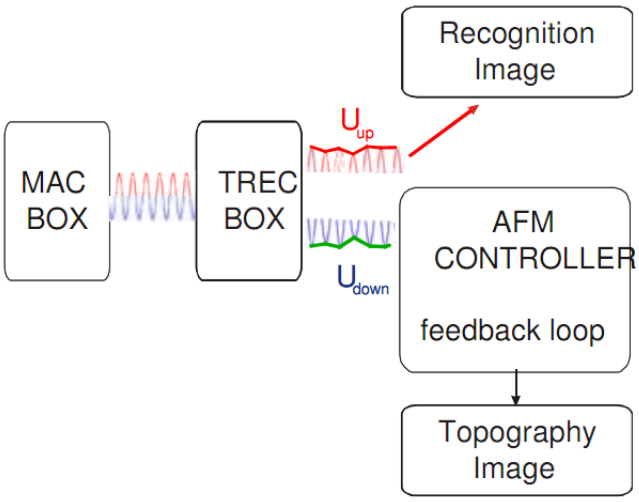

Figure 11. An illustration of the PicoTREC system. An oscillating cantilever gives signal and first it goes to the MAC box. From there it travels to PicoTREC box which then separates the signal according to amplitude and creates a recognition image and topographical map [52].

2.6 Advantages & shortcomings

Unlike SEM, AFM provides three dimensional surface profile (instead of two-dimensional image). In sample preparation any kind of special treatments are not needed (e.g. labeling or fixation). This includes coating sample with conductive material which could damage the sample. Also constant vacuum do not have to be maintained in order to make measurements. AFM works properly in different physiological environments and it has various tips for different purposes like MAC mode and FS. Additionally dynamic processes can be imaged with AFM.

Despite the fact that AFM has many advantages over other imaging modalities, it also has its weak points. In AFM only images around 150×150 µm^2 with a maximum height being 10-20 µm can be scanned (in SEM the scanning area is around 1 mm^2). Scanning speed is also slow when high resolution images are preferred. It takes typically several minutes to acquire a typical an image with AFM whereas in SEM

images can be acquired in almost real time. Scanning speed is known to induce thermal drifting to images. Besides drifting, AFM image can also have traditional artefacts that can come from environment, tip or sample itself. In contact mode sample may alter degradation during imaging since the tip is in contact all the time.

3 Optical fluorescence microscopy

In the last decade, fluorescence microscopy has evolved from a classical microscopy approach into an advanced imaging technique that allows the observation of cellular activities in living cells with increased resolution and dimensions. Besides new imaging concepts like STED and PALM, progress has been made also in the field of components. Optical fluorescence microscopy is the most common way to study molecular activities happening inside the cell.

3.1 Basics in optical microscopy

3.1.1 Numerical aperture

Numerical aperture (NA) is a dimensionless measure of lenses ability to gather or emit light and it is one of the most important terms in optical microscopy. Abbe was the first person to define this term [10] and it can be expressed in mathematical form as follows

$$NA = n \sin \alpha, \tag{8}$$

where n is the refractive index of the medium and α is the one-half angular aperture of the objective. Higher numerical aperture means that more light goes into the objective. Higher NA is achieved by widening the angle α or increasing the refractive index of the medium. The maximum cone angle is 90 degrees and by inserting this to the equation 8, the theoretical maximum value for numerical aperture is the refractive index of the immersion medium.

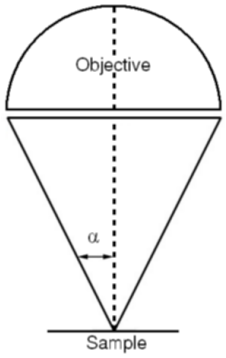

Figure 12. The numerical aperture of the objective, where α denotes the angle between the diffracted light ray and the surface normal.

In air the theoretical maximum for numerical aperture is 1 and with oil immersion lenses numerical aperture of 1.44 can be reached. Water can be also used as an immersion medium with a refractive index of 1.33. Manufacturers have optimized their objectives for specific immersion mediums so it is important to use manufacturer recommended immersion mediums to avoid optical mismatching. If optical density changes between mediums, the light will refract (see fig. 13).

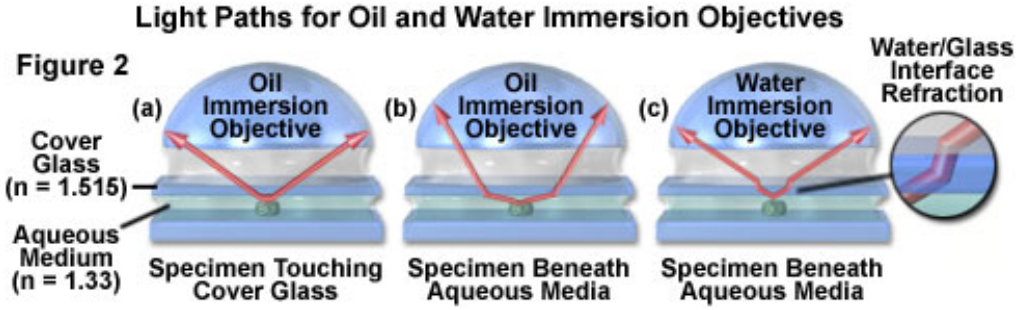

Figure 13. Illustration how refractive indexes affect to lights path. In (a) and (b) the immersion medium is oil and in (c) water [54].

3.1.2 Resolution

In the article which Abbe published in 1874 [10], he explained how the wavelength is related to image formation and what are the physical limitations for resolution. The sample can be thought to be a lattice which then diffracts the illumination light. Small samples have small details which means bigger diffraction of the light. The

greater the number of higher diffracted orders of light admitted into the objective, the smaller the details of the specimen that can be clearly separated. Since the numerical aperture of the objective is limited, some of the diffracted light will always miss the objective. Direct and diffracted light will be gathered into the objective and objective projects the light to the image plane of the eyepiece diaphragm in the form of small, circular diffraction disks known as Airy disks. Abbe showed in his experiments that sharpness of the image is related to the amount of light coming into the objective. From his experiments Abbe derived his famous equation

$$d = \frac{\lambda}{2NA}, \tag{9}$$

where d is the minimum resolving distance, λ is the wavelength of the used light and NA is numerical aperture. Equation 9 is the limit of resolution in its simplest form.

The resolution of a microscope is the ability to clearly separate two objects as distinguished entities by the observer or the camera. These points appear as Airy diffraction patterns (Airy disks) in the image plane where the intensity maximum is in the middle (see fig. 14) [55, 56]. When looking Airy diffraction pattern from the side and along the image plane it forms a curve which is called point spread function (PSF). This curve represents the intensity distribution in focal plane. Mathematical formula for PSF is

$$h(\nu) = A \cdot \left| \frac{2J_1(\nu)}{\nu} \right|^2, \tag{10}$$

where A is a constant, J_1 is the Bessel function of the first kind of order one, and ν is optical unit in focal plane. In terms of wavelength and resolution, the optical unit is described

$$\nu = \frac{2\pi r NA}{\lambda}, \tag{11}$$

where r is the distance from the focal point, NA is the numerical aperture and λ is wavelength. Numerical aperture is defined as a product of refractive index n and

$\sin\alpha$, where α is the half-angle of the maximum cone of light that can enter the objective. Resolution limit and point spread functions are presented in figure 14.

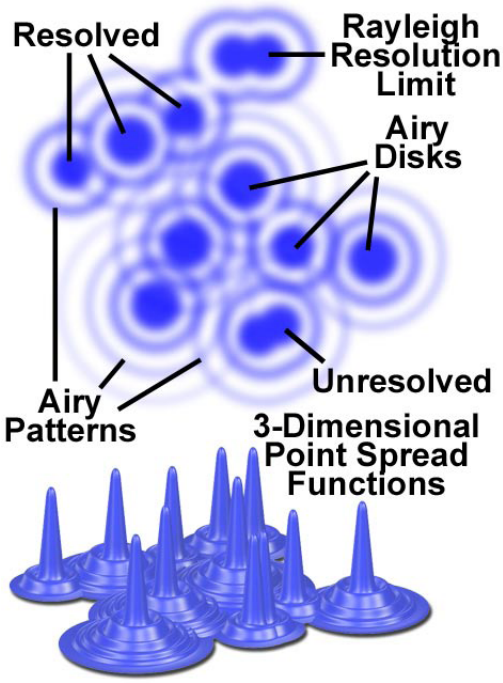

Figure 14. Airy patterns and the limit of resolution. Resolved and unresolved Airy Disks are presented in the picture same as the Rayleigh's criteria [57].

When Airy patterns start to go one on top of the other and these two intensity peaks are barely separated from each other, Rayleigh's criteria is reached [58]. Mathematically this limit is reached when the maximum of one point source coincides with the first minimum of the other (see fig. 15). The first minimum of J_1 is located at $\nu = 3,8317$ [59]. From this the formula for resolution can be derived (also known as Abbe's equation)

$$\nu = \frac{2\pi r NA}{\lambda} = 3.8317 \Rightarrow r = \frac{3,8317 \cdot \lambda}{2\pi \cdot NA} = \frac{0.61 \cdot \lambda}{n \sin\alpha}, \tag{12}$$

where r is resolution limit, λ is the wavelength of the light, n is the refractive index and α is the one-half angular aperture of the objective. The constant 0.61 is the first minimum of J_1 divided by 2π. From this equation the limit of resolution for standard confocal microscope can be calculated. With confocal microscope resolution of 170-200 nm can be achieved depending on the wavelength used.

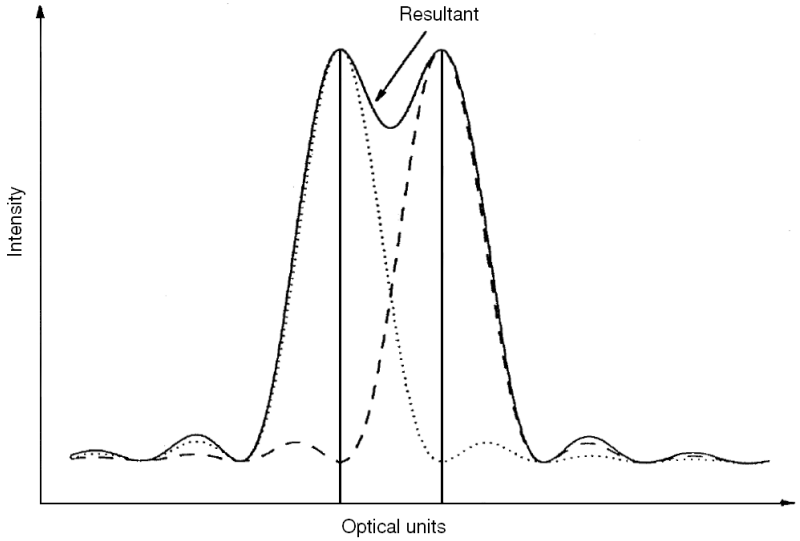

Figure 15. Principle image of Rayleigh's criteria. When the maximum of one point source coincides with the first minimum of the other, points can not be separated as 2 different points.

3.1.3 Structure of a microscope

After Hooke designed his microscope, the structure of microscope has been staying quite the same. Modern optical microscopes still have the same key pieces, which Hooke had in his microscope apparatus [6].

The configuration for a basic light microscope is simple. In old microscopes light source was candle flame (like in the figure 1) or normal day light, which was directed with a mirror to the sample. Nowadays light is generated with e.g. a tungsten lamp or light emitting diodes (LEDs).

The amount of light coming from the light source is limited with a field diaphragm. The size of the iris determines how much light can go through and it works same way as an iris of the human eye. When making the aperture smaller, also the field of view (FOV) gets smaller. When FOV is small, aberrations in the image are reduced since the light is getting through only from the middle of the lens where aberrations are less significant.

After "good" part of the light is selected with diaphragm, it is focused onto the sample with a condenser. The condenser is a group of lenses that are always located

between the light source and the sample stage. Modern light microscope condensers are following the design of Abbe condenser. Next in light's path is a sample, which lies on the sample stage. Either the sample stage is moved up and down when focusing with focusing controls or the objective is either raised or lowered and the sample stage is staying still.

An objective consists of several lenses inside a tube. It gathers the light from that is coming from the sample and directs it onwards to a detector. This can be a human eye, a CCD-camera or a photomultiplier tube (PMT), for example. Objectives are designed for different immersion mediums like air, water and oil (different refractive indexes).

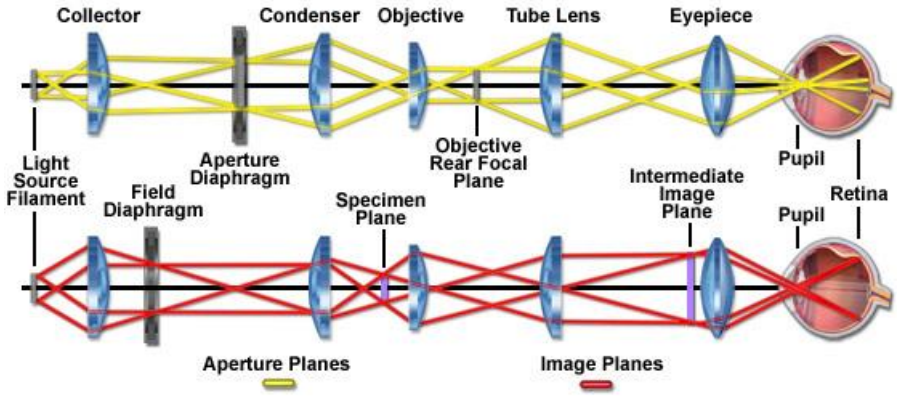

Figure 16. Köhler illumination generates an extremely even illumination to the sample plane. This method also ensures that an image of the illumination source do not appear on the resulting image which was a problem in older illumination methods [60].

3.1.4 Confocality

First confocal microscope was patented in 1955 by Marvin Minsky [61]. This method is common in fluorescence microscopy. In confocal setup (fig. 17) there is a pinhole in front of the detector which allows light only from focus spot to reach the detector. This increases the depth resolution compared to wide-field microscopes since it eliminates light that comes from other planes except focal. Also the excitation of fluorophores is done with a laser (with a pinhole aperture) instead of even illu-

mination light from below the sample. Although a pinhole gives better resolution, it also makes the acquired signal weaker. Despite of this, confocal microscopes are standard in imaging because they can produce 3D-images.

The most significant difference between confocal and wide-field microscope is the image formation. In confocal microscope you illuminate only one diffraction limited spot with a laser and image is formed after scanning the whole sample point by point. In normal wide-field microscope all of the sample plane is illuminated at the same time.

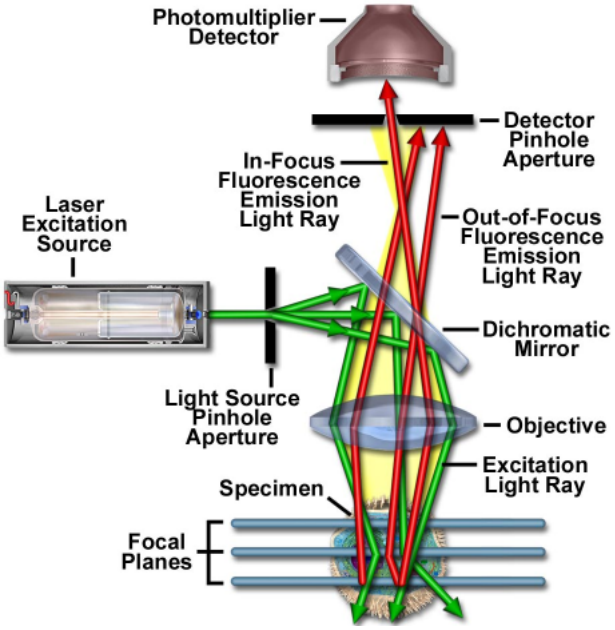

Figure 17. The pathway of the light and the principle of a confocal fluorescence microscope. Laser light is directed to the objective with a dichromatic mirror (beam splitter) and emission light goes through the beam splitter. A pinhole in front of the detector blocks emission light that is not coming from focal plane [57].

3.2 Fluorescence

3.2.1 Photoluminescence

Photoluminescence is a process where molecule absorbs energy in a form of photons (electromagnetic radiation) and re-radiates photons. After absorbing the photons molecule will go to excited state, which is referred to as lowest unoccupied molecu-

lar orbital (LUMO). This means that electron will jump from ground state (highest occupied molecular orbital, HOMO) to a singlet state (S_N), which has more energy due to photon absorption. This state is unstable and electron will soon relax back to ground state. Another option for electron relaxation is triplet state, which is more stable than the singlet state. Excess energy is either emitted as electromagnetic radiation (radiative process) or through non-radiative processes like internal conversion or vibrational relaxation.

Emission photon can have the same energy as the photon that originally excited the molecule (in theory) but usually one part of the excitation energy is lost to heat and vibration. If the relaxation happens really fast, process is considered as fluorescence. If emission comes from triplet state, process is called phosphorescence. Main difference in these two processes is the time interval. In fluorescence the photon emission happens within nanoseconds (excluding delayed fluorescence) where as in phosphorescence photon will be emitted within seconds after excitation.

3.2.2 Properties of fluorescence

Different excitation and relaxation processes are usually described with Jablonski diagrams. In figure 18 there is a Jablonski energy diagram with 4 different molecular orbitals marked as S_0, S_1, S_2 and T_1. For a molecule, several different energy states exist depending on total energy and spin states of the electrons in the molecule. If electrons have opposite spins, the state is called singlet. These states are referred with letter S_N. Each of these states has sub-levels according to vibrational and rotational energies. Because excitation usually happens without changes in spin orientation, the excited state is singlet. Internal conversion and vibrational relaxation are processes where the excited state loses its energy to the environment. When electron relaxes to T_1 after it has been excited to singlet state, it is referred as intersystem crossing. Relaxation from singlet to triplet state has a very low probability

due to spin orientations.

One relevant rule in understanding emission is Kasha's rule. A molecule can be excited to different singlet states (S_2, S_3,...) but according to the rule, appreciable yield of photon emission comes only from the lowest excited state. Since only one state is expected to yield emission, an equivalent statement of the rule is that the emission wavelength is independent of the excitation wavelength [62].

Difference in absorption and emission band maxima is called Stokes shift. Excitation wavelength is shorter than emission wavelength, because energy is lost to heat and as vibrational energy between excitation and emission. Bigger shift is better in spectroscopy since it makes the detection of emission easier from the absorption spectra. Stokes shift is presented in figure 18.

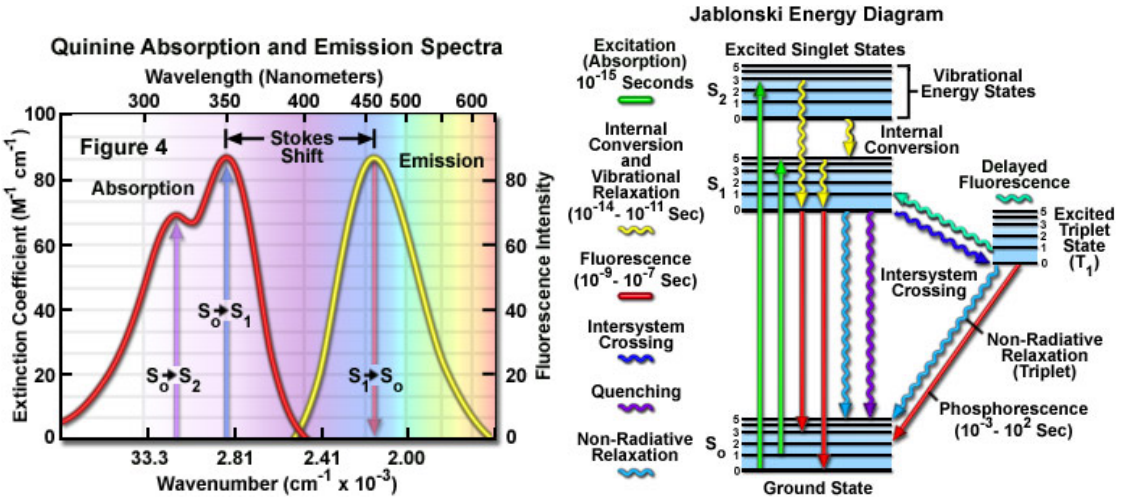

Figure 18. Stokes shift on the left. If the emission photons have more energy than absorbed photons, then this difference is called anti-Stokes shift. Different processes in excitation and relaxation are presented in the Jablonski energy diagram. Fluorescence is not the only relaxation process and it "competes" with the other processes. Also excitation can happen to other singlet states as shown in the diagram [63].

Quantum yield describes the efficiency of the fluorescence process. Maximum value is 1 (or 100 %) and it is simply described

$$Q = \frac{\text{Number of photons emitted}}{\text{Number of photons absorbed}}. \tag{13}$$

We can also use decay rates to quantify the the efficiency of the fluorescence:

$$Q = \frac{\Gamma}{\Gamma + k_{nr}}, \tag{14}$$

where Γ is the emissive rate of the fluorophore and k_{nr} is the rate of nonradiative decays such as internal conversion [64].

Lifetime for fluorescence is defined as the average time the molecule stays in its excited state before emitting the excess energy. Equation for lifetime can be expressed

$$\tau = \frac{1}{\Gamma + k_{nr}}, \tag{15}$$

where k denotes different constants for nonradiative decay pathways. Generally fluorescence lifetimes are in the range of nanoseconds [64].

3.2.3 Immunofluorescence

Immunofluorescence uses the specificity of antibodies to their antigen to label specific parts in cells. There are two kinds of staining methods. First one is the direct staining where the primary antibody is labeled with fluorescence dye. Second one is indirect, where fluorescence labelled secondary antibody is used to recognize a primary antibody.

Because of the biological nature of this method, labeling is not always perfect and antibodies can bind themselves nonspecifically. Common problems in immunofluorescent labelling are quenching and bleaching. Quenching decreases the fluorescence intensity of the sample and it can be a product of various things. These include energy transfer, complex-formation, excited state reactions and collisions. Quenching is used in Förster resonance energy transfer (FRET) in fluorescence microscopy but in normal fluorescence imaging it is disadvantageous [65].

Photobleaching means destruction of fluorophore. This happens due to photon-induced chemical damage which alters the structure of fluorescent molecule and

excited state of the fluorophore is highly reactive. Normally imaging is done in a dark room and samples are preserved in a container to minimize the unnecessary light exposure. Like quenching, photobleaching can also be used in imaging. This technique is called fluorescence recovery after photobleaching (FRAP) [66].

3.3 STED fluorescence microscope

Theory of the STED microscope was first published in 1994 by Stefan Hell [22]. The basic idea in STED is to selectively inhibit the fluorescence in outer parts of the focal spot by making molecules go back to ground state. This is done by stimulated emission with a second laser. Stimulated emission is a process where excited molecular state relaxes to ground state when interacting with an electromagnetic wave. The released photons have the same phase, frequency, polarization, and direction of travel as the photons of the incident wave [67].

In figure 19 there is the basic and simplified setup for STED microscope. It consists of 2 lasers (excitation and depletion laser), detector, lenses and a phase plate as seen in the picture. First sample is illuminated with a laser which excites the molecules into excited state. This can be seen as the first phase. In second phase we apply another laser, which is named depletion beam, to "switch off" fluorescence from the edges of the excitation spot. Also we want to modify depletion beam in a way that the centre of the second pulse has an intensity of zero. This is done by vortex prism and it modifies the beam so that it looks like a doughnut [68]. Reducing the extent of the focal spot is commonly called PSF engineering.

3.3.1 Excitation phase

Every molecule is in ground state before applying the excitation laser. After the excitation is done, molecules are in singlet state. Singlet state has sub-levels which have different vibrational energies (S_n^{vibr}). These vibrational levels have the lifetime

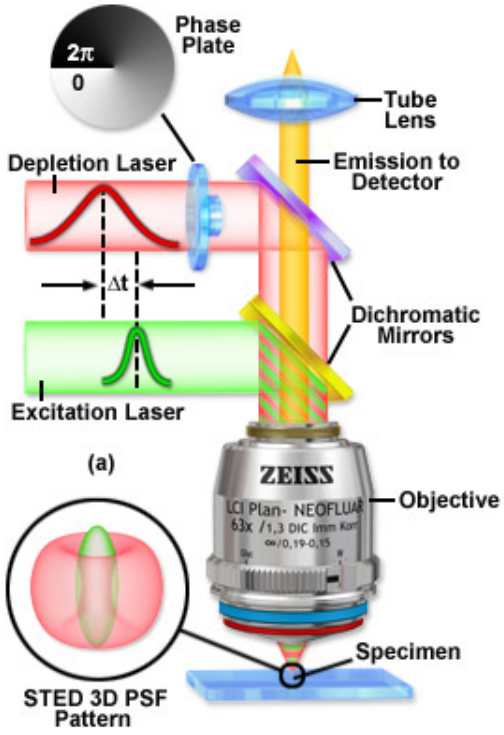

Figure 19. A basic setup for a STED microscope. Modern STED microscopes utilize vortex prisms instead of phase plates. Δt is the interval between the excitation and STED pulse. This can be adjusted within the software [69].

of less than 1 ps and after excitation fluorophore is almost immediately on its relaxed state of S_1. To inhibit fluorescence S_1 needs to be depopulated since this state is the actual source of fluorescence photons. Population densities for different states can be expressed as differential equations which describes different fluorescence processes like thermal quenching, vibrational relaxation and spontaneous emission:

$$\frac{\mathrm{d}n_0}{\mathrm{d}t} = h_{\mathrm{exc}}\sigma_{\mathrm{exc}}(n_1^{\mathrm{vib}} - n_0) + k_{\mathrm{vib}}n_0^{\mathrm{vib}} \tag{16}$$

$$\frac{\mathrm{d}n_0^{\mathrm{vib}}}{\mathrm{d}t} = h_{\mathrm{sted}}\sigma_{\mathrm{sted}}(n_1 - n_0^{\mathrm{vib}}) + (k_{\mathrm{fl}} + k_{\mathrm{Q}})n_1 - k_{\mathrm{vib}}n_0^{\mathrm{vib}} + k_{\mathrm{ph}}n_2 \tag{17}$$

$$\frac{\mathrm{d}n_1}{\mathrm{d}t} = k_{\mathrm{vib}}n_1^{\mathrm{vib}} + h_{\mathrm{sted}}\sigma_{\mathrm{sted}}(n_0^{\mathrm{vib}} - n_1) - (k_{\mathrm{fl}} + k_{\mathrm{Q}} + k_{\mathrm{isc}})n_1 \tag{18}$$

$$\frac{\mathrm{d}n_1^{\mathrm{vib}}}{\mathrm{d}t} = h_{\mathrm{exc}}\sigma_{\mathrm{exc}}(n_0 - n_1^{\mathrm{vib}}) - k_{\mathrm{vib}}n_1^{\mathrm{vib}} \tag{19}$$

$$\frac{\mathrm{d}n_2}{\mathrm{d}t} = k_{\mathrm{vib}}n_2^{\mathrm{vib}} - k_{\mathrm{ph}n_2} \tag{20}$$

$$\frac{\mathrm{d}n_2^{\mathrm{vib}}}{\mathrm{d}t} = k_{\mathrm{isc}}n_1 - k_{\mathrm{vib}}n_2^{\mathrm{vib}} \tag{21}$$

where the $\sum_i n_i(\nu, t) = 1$. The rates for excitation and stimulated emission are given by the product of the photon fluxes of the beams and molecular cross sections ($h_{\text{sted}}\sigma_{\text{sted}}$, for example). Typical values for σ_{exc} and σ_{sted} are $10^{-16} - 10^{-18}\text{cm}^2$. k is the coefficient for different spontaneous processes and it is given by inverse of the lifetime. This coefficient for fluorescence is defined $k = 1/\tau_{fl}$, for example. In order to stop the spontaneous relaxation from singlet state to ground state, excited state should be quenched with a stimulating beam.

3.3.2 Depletion phase

Depletion by stimulated emission (light quenching) has three competing processes. These processes can be taken from our previous equation 16-21 and they are:

$$h_{\text{sted}}\sigma_{\text{sted}}n_1 \quad >> \quad k_{\text{vib}}n_1^{\text{vib}} \tag{22}$$

$$h_{\text{sted}}\sigma_{\text{sted}}n_1 \quad >> \quad (k_{\text{fl}} + k_{\text{Q}} + k_{\text{isc}})n_1 \tag{23}$$

$$h_{\text{sted}}\sigma_{\text{sted}}n_1 \quad >> \quad h_{\text{sted}}\sigma_{\text{sted}}n_0^{\text{vib}}. \tag{24}$$

First competing process is the supply from the higher vibrational levels of S_1^{vib} given by $k_{\text{vib}}n_1^{\text{vib}}$. Second mechanism is spontaneous decay, which is denoted $(k_{\text{fl}} + k_{\text{Q}} + k_{\text{isc}})n_1$. These two mechanisms can be outperformed by using pulsed lasers. STED pulse comes immediately after excitation pulse so S_1 is not supplied from S_1^{vib}. To avoid spontaneous emission, stimulating pulse has to follow closely the excitation pulse. High intensity of the STED beam is required in order to surpass spontaneous emission. Pulse duration is restricted and the duration comes from the last competing mechanism, re-excitation, which is denoted $h_{\text{sted}}\sigma_{\text{sted}}n_0^{\text{vib}}$. If there is a high population in n_0^{vib} when quenching S_1, pulse will re-excite the dye to the first singlet state. This means that the stimulated emission rate should be low enough to allow S_0^{vib} to relax. Lifetime of vibrational states is ≤ 1 so duration of STED pulse should be in range of several picoseconds. Longer duration in depletion increases efficiency of the depletion because of the higher intensity. Continuous wave (CW)

lasers can be used for depletion [70, 71], although pulsed lasers are preferred because they are effective and they induce less photobleaching.

The shape of the STED beam is important since we only want to switch off the dye from the edges of the focal spot. The shape is made with a vortex prism that creates optical vortex (a doughnut) which has zero intensity in the middle. The representation of the beams and focal spot are illustrated in figure 20.

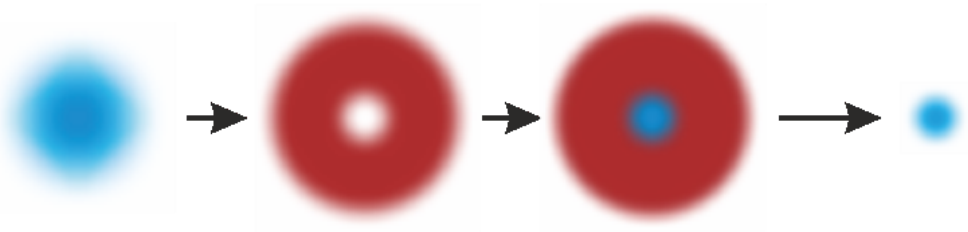

Figure 20. Blue spot represents the normal fluorescence spot after exciation. Next one is the STED beam after it has passed the vortex prism. Beams are aligned in a way that the STED beam sweeps of the outer fluorescence from the edges of excitation spot and small spot is left.

The PSF of a STED fluorescence microscope can be calculated by solving the differential equations (14-19) and assuming that beams are pulsed and the STED pulse comes immediately after the excitation pulse. Pulses should have Gaussian temporal pulse shape [22]. Three dimensional point spread functions of the surface are presented in figure 21 and the pulse shapes are defined:

$$h_{\mathrm{exc}}(\nu,t) = \tilde{h}_{\mathrm{exc}}(\nu)e^{-((t-t_0)/\tau_p)^2\ln 2} \quad (25)$$

$$h_{\mathrm{sted}}(\nu,t) = \tilde{h}_{\mathrm{sted}}(\nu)e^{-((t-t_0)/\tau_p)^2\ln 2}, \quad (26)$$

where h is the PSF and τ_p is the pulse duration. Optical unit ν is defined $\nu = 2\pi nr\sin\alpha/\lambda$ with $r = \sqrt{x^2+y^2}$ and t is respective time point.

The dependency between fluorescence signal and intensity of the STED beam is also shown in figure 21. From the slope it is seen that the intensity of the beam can be increased to infinity in theory but increase in the laser power weakens the fluorescence signal. And when targeting huge amount of energy into a really small spot, fluorescent dye is damaged.

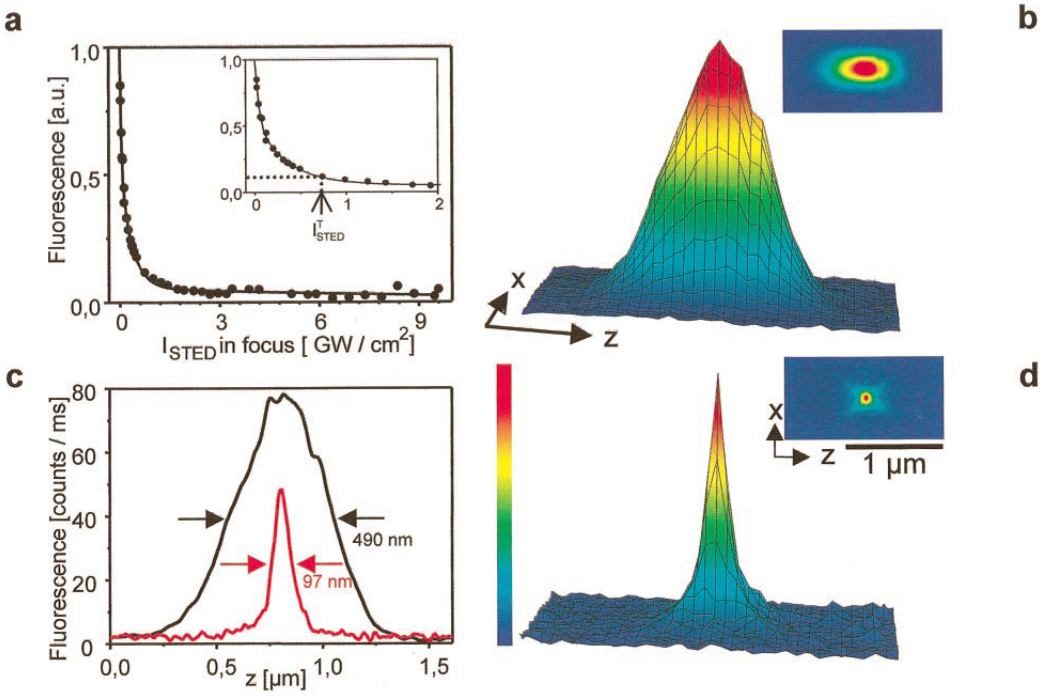

Figure 21. (a) shows the fluorescence as a function of intensity. In (b) there is the surface plotted from confocal fluorescence spot and (d) is the same as (b) but STED beam is switched on. In (c) there are intensity profiles (PSFs) from (b) and (d) [70].

After the principles of STED microscope was published in 1994, general theory for bypassing the resolution limit was introduced. This technique is named reversible saturable optical fluorescence transitions (RESOLFT). The idea in this technique is to have two distinguishable states in a molecule (A and B) and populations of these states are controlled. In other words fluorescent molecule can be switched off and determine where fluorescence is allowed. Every method that uses these two states to bypass the resolution limit are considered to utilize RESOLFT.

In RESOLFT, the minimal resolvable distance between two points can be expressed with equation

$$\Delta d = \frac{\lambda}{2n \cdot \sin\alpha \cdot \sqrt{1 + \frac{I}{I_{sat}}}}, \tag{27}$$

where Δd is the minimal distance, λ is wavelength, n is refractive index, α is the one-half angular aperture of the objective, I_{sat} is the characteristic intensity required for saturating the transitions and I is the applied intensity. Equation 27 can be seen

as the extension of equation 9. To achieve better resolution, the factor $\zeta = I/I_{sat}$ has to be increased [72, 73].

Samples for STED microscope are prepared in the same way as in normal confocal fluorescence microscope (see chapter about samples). When choosing fluorescent dye, information about the wavelength of excitation laser is needed. STED beam should not excite the molecules. Also information about the emission wavelength is needed in order to have the right depletion wavelength. STED microscope has a high resolution so thickness-corrected cover slips should be used and embedding medium should have a refractive index as close as possible to 1.51 to prevent optical mismatch.

Experimental part

4 Introduction

Osteoporosis is a chronic disease and it is defined by a decrease in bone mineral density. This is due to an imbalance of the bone remodeling cycle [74]. This imbalance can be caused by decreased osteoblast activity (in normal cases) or increased osteoclast activity. Imbalance weakens the bone and therefore makes the skeletal structure more fragile and more vulnerable to fractures, effects seen predominantly in older population. Dual X-ray absorptiometry (DXA) is used to determine if a person has osteoporosis. DXA devices measure the bone mineral density (BMD) and these values are compared to different population distributions to acquire T-score and Z-score. DXA measurement gives the peak bone mass of the person and it is compared to the statistical BMD of population's young healthy adults. If the BMD is less than 2.5 standard deviations from the peak bone mass (T-score of -2.5), person is suffering from osteoporosis [75, 76].

Current treatments for osteoporosis include agents like bisphosphonates and re-

ceptor activator of nuclear factor κ-B ligand (RANKL) inhibitors. Bisphosphonates kill osteoclasts but they also kill other bone cells and are shown to cause osteonecrosis of the jaw if taken in high dosage [77]. Denosumab mimics the activity of osteoprotegerin and it binds to RANKL. This prevents RANKL interacting with receptor activator of nuclear factor κ B (RANK). In clinical studies with humans this is shown to reduce bone resorption [78]. For menopausal women estrogen replacement therapy is used for some cases. This therapy replaces hormones which the ovaries no longer produce and it is shown to prevent bone loss [79, 80].

The renewal of bone is a process that occurs throughout a person's life. Old bone is removed and new is formed when body is repairing microfractures in the bone that come from everyday life. This cycle starts when preosteoclasts get the activation signal and start to differentiate into mature osteoclasts under the influence of cytokines and growth factors e.g. macrophage colony-stimulating factor (M-CSF) and RANKL [81, 82]. Matured osteoclasts attach themselves to the bone surface and resorb a discrete area of the mineralized bone matrix. Osteoprogenitor cells (preosteoblasts) then migrate into the resorption area and stop the osteoclast activity. Osteoprogenitor cells are differentiated into osteoblasts and they start to deposit new bone matrix into the resorption pit until it is filled. Osteoblasts that are embedded into the new bone matrix, will mature into terminally differentiated osteocytes. Bone resorption takes around 2-3 weeks and bone formation is significantly slower and can take up to 4 months to fully restore the bone structure [83]. This cycle is illustrated in the figure 22.

Osteoclast ligand binding to the bone surface involves the interaction of the integrin receptor $\alpha_V\beta_3$ with ECM proteins within the bone matrix [85]. Integrins are membrane glycoproteins, composed of an α- and a β-subunit. $\alpha_V\beta_3$ recognizes the arginine-glycine-aspartate (RGD) sequence in osteopontin and attaches osteoclast to the bone surface. However recent unpublished results indicate that other fac-

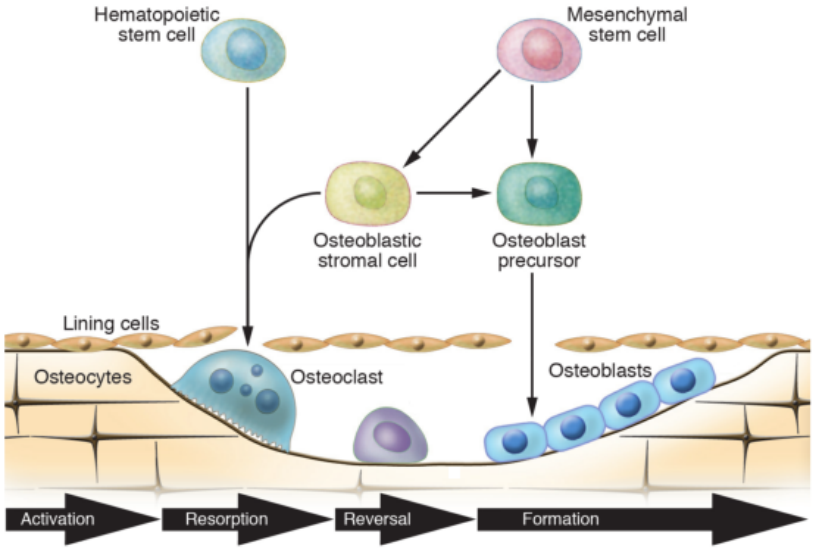

Figure 22. The bone remodelling cycle is divided into four sections (arrows in the bottom). First is the activation phase when stem cells receive a signal and start to differentiate. Then comes resorption phase where osteoclasts resorb the bone matrix. After this comes brief reversal phase where bone surface is covered with mononuclear cells but bone formation has not started. Bone formation is the last phase and includes waves of osteoblasts which eventually terminally differentiate into osteocytes or undergo apoptosis [84].

tors besides integrin contributes to the binding since osteoclasts still attach even if the integrin binding is blocked. By labelling integrin and cellular proto-oncogenic tyrosine kinase (c-Src), osteoclast binding and active $\alpha_V\beta_3$ can be seen in the fluorescence image. AFM brings out the dimensions of the cell and it is possible to see small bone fragments inside the osteoclast resorption cavity. When using force spectroscopy, detailed information about the forces that are involved in the binding can be acquired.

The purpose of our experiment setup is to create a tool to study these interactions in detail with two microscopes. If this is done separately, it is hard to find the exact same place from the sample with both microscopes. To prevent this problem, 2 microscopes were merged and this made possible to image same area from the sample at the same time without moving the sample between image acquisition.

5 Materials and methods

5.1 Samples

5.1.1 Samples for system calibration

Before imaging with biological samples, multiple test samples were made to study the imaging with both modalities. These test samples had two requirements: they should be fluorescent and they should be visible in AFM image. First test samples included nanodiamonds (ND) that were acquired from General Physics Institute (Moscow, Russia). The most common synthesis methods to produce nanodiamonds are chemical vapor deposition (CVD) and detonation [86, 87]. In CVD diamond film is synthesized on a substrate in a gas mixture. By changing gasses and their ratio, properties of the diamond can be altered. In detonation synthesis carbon containing explosives are used, mainly trinitrotoluene (TNT) and a custom designed research department explosive (RDX).

All of our ND samples were made by detonation synthesis but the sample treatment varied between the samples. In ND1, diamonds were purified with acid and then functionalized by siliceous grain aminopropyl-triethoxysilane (APTES). ND aggregates in the sample (using H_2O and ethanol as solvent) varied from 100-1000 nm. ND4 was functionalized by carboxyl groups using combination of H_2O and ethanol (50:50) as solvent. Typical size of the diamond aggregates in this sample were between 1000-5000 nm. In ND5 size of the aggregates were approximately 200 nm after acid purification and used solvent was H_2O. In sample that was labelled "30 nm", large aggregates were removed from ND5 by centrifugation.

Acquired ND samples were diluted in ethanol with different concentrations (see table I). The original sample concentrations were 0.5 mg/mL but they were said to be very indicative. Before making the solution, ND samples were sonicated with tank and tip sonicator. First tube contained 5 µL of ND sample and 495 µL of

ethanol. This was diluted again so the concentrations were 1:100 and 1:10^4. 10 µL of dilutude samples were pipetted to cover slip in a way that it covered entire cover slip. Then the samples were left to dry. After 30 minutes samples were ready to image with the STED/AFM-combination.

6 samples including 2 different quantum dots (Qdots) were made in several dilutions (see table I). Samples were made from Qdot® 525 streptavidin conjugate (Qdot525) by Invitrogen (Hayward, USA) and Qdot® 625 ITK™ carboxyl quantum dots (Qdot625) also from Invitrogen (Eugene, Oregon, USA). The original concentration for Qdot625 was 8 µM in 50 mM borate (pH 9.0) and for Qdot525 1 µM. Both samples were diluted in ion-exchanged water (mQ H_2O). Sonication was done before and after diluting. First tube contained 1 µL of Qdots and 99 µL of water so the dilution was 1:100. 5 µL of the sample was pipetted to the cover slip and were left to dry. After 30 minutes samples were ready for imaging.

Third set of samples contained fluorescent beads BF530 with diameter of 85 nm by ArcDia (Turku, Finland) and carboxylate-modified microspheres (Fluospheres®) manufactured by Invitrogen (Eugene, Oregon, USA). The diameter of these microspheres was 0.175 ± 0.005 µm and they are excitable at 540 nm. The density in suspension (1 mL) was approximately 3×10^9 beads/mL. First cover slips were coated with 0.1 mg/ml poly D-lysine and they left to dry in room temperature (RT) for 30 minutes. Then the cover slips were washed three times with approximately 1 mL of phosphate buffered saline (PBS) and once with ion-exchanged water. BF530 was diluted in PBS (with ratios 1:10^3 and 1:10^5) and Fluospheres® was not diluted at all. To remove residual salt, cover slips were washed with water after the sample was pipetted to cover slip.

Table I. Dilution ratios for different samples and solvents used.

Sample	Solvent	1:1	1:10	1:100	$1:10^3$	$1:10^4$	$1:10^5$	$1:10^6$
ND1	Ethanol			x		x		x
ND4	Ethanol	x		x				
ND5	Ethanol	x		x				
ND5	mQ H_2O			x		x		x
ND 30nm	Ethanol	x		x				
Qdot525	mQ H_2O			x	x		x	
Qdot625	mQ H_2O			x		x		x
Qdot625	PBS				x		x	
BF530	PBS			x	x		x	
Fluospheres®	-	x						

5.1.2 Osteoclast samples

Osteoclasts that were used in this experiment were differentiated from mesenchymal stem cells. To activate the resorption mechanism, they were exposed to milled submicron bovine bone particles. This exposure time was changed between samples ranging from 0 minutes to 3 hours.

First cover slips were cleaned with ethanol and water. Then differentiated osteoclasts were transferred to cover slips and they were given enough time to attach to the surface of the cover slip, approximately 2 hours. Two sets of samples were made. First set contained osteoclasts with bone particles (5 µL) and the second set did not have any bone particles in it. Used time points were: 0 min, 5 min, 10 min, 20 min, 1 h and 3 h. When desired time point was achieved, sample was fixed with 500 µL of solution that contains 3 % paraformaldehyde (PFA) and 2 % sucrose for 15 minutes. After this samples were stored in PBS in a high volume at +4 °C.

Staining was done next. In order to get the solutions inside the cell, samples

were permeabilized 5 minutes on ice by adding 500 µL of mixture containing 20 mM 4-(2-hydroxyethyl)-1-piperazineethanesulfonic acid (HEPES), 300 mM sucrose and 50 mM sodium chloride (NaCl). In addition 0.5 % of the mixture was Triton X-100. To prevent unspecific binding of antibodies, samples were blocked with 500 µL of 3 % bovine serum albumin (BSA) in PBS. After 10-20 minutes the solution was removed. Used primary antibodies were $\alpha_V\beta_3$ from USBiological (Swampscott, Massachusetts, Clone No 2Q880) and c-Src(SRC 2):sc-18 from Santa Cruz Biotechnology (California, USA). They were both diluted in 500 µL of 0.5 % BSA in PBS -solution. Both dilutions were added to the well (total volume 1000 µL) and the samples were incubated 1 hour in RT. After this the samples were washed (5 min) three times in PBS in a large volume. Next 500 µL of the diluted secondary antibodies (1:1000), Chromeo™494 Goat anti-Mouse IgG from Active Motif (Carlsbad, CA, Lot#: 15410001) and Atto 647 goat anti-mouse IgG (whole molecule) from Sigma-Aldrich (Buchs, Switzerland) were added in 0.5 % BSA in PBS -solution. Then the samples were incubated in dark and RT for 45 minutes. For nuclei staining Quant-iT™ PicoGreen® dsDNA reagent from Invitrogen (Eugene, Oregon, USA. Lot: 32308W) was added (5 µL) to the well that already contained 1000 µL of secondary antibody and the samples were incubated 10 minutes. Finally the samples were washed three times (5 min) in PBS (large volume in dark). The prepared samples were stored in the refrigerator (+4 °C) in PBS.

5.2 Experimental setup

5.2.1 AFM

For topographical imaging AFM (Agilent 5500 SPM, Agilent Technologies Inc.) was used. To image samples in fluid, contact, tapping and MAC mode were available. With PicoTREC molecular recognition imaging system specific binding studies were possible. Software used to control the microscope was PicoView 1.10.1 (Agilent

Technologies Inc.). The cantilever bending is detected using infra red laser (750-900 nm) and suitable quadrupole photodetector. This way the laser does not interfere with fluorescence imaging. The stage where AFM is implemented is manufactured by Molecular Imaging and it is originally designed for Zeiss invert microscopes.

5.2.2 Confocal fluorescence microscope

Fluorescence imaging was done with Leica TCS SP5 (Mannheim, Germany) which had super-resolution extension (Leica TCS STED) installed. To control the microscope LAS AF software (Leica Microsystems) was used. To detect emission, total of 7 detectors were available: 4 internal photomultiplier tubes (PMT), 1 external Leica HyD detector (GaAsP (Gallium arsenide phosphide) hybrid detection system) and 2 external avalanche photodiodes (SPCM-AQRH-13 from PerkinElmer). For normal confocal excitation typical visible spectrum wavelengths were available ranging from 458 nm to 633 nm. For STED excitation, external pulsed diode lasers LDH-P-FA-530B (λ= 531 nm) and LDH-P-C-640B (λ= 635 nm) from PicoQuant (Berlin, Germany) were available. The depletion beam was generated with Mai Tai Ti:Sapphire oscillator (The Spectra-Physics, Irvine CA, USA) ranging from 680 nm to 1040 nm.

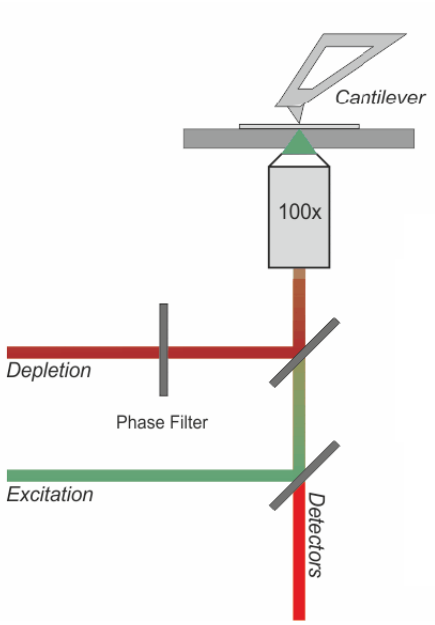

Figure 23. Illustration of our experimental setup. Fluorescence imaging is done from the below while AFM scans the surface.

5.3 AFM probes

NSC19 - tapping mode (intermittent contact)

19 series tips are made from n-type silicon doped in phosphorus by MikroMasch (Tallinn, Estonia). They are made by etching and the 19 series tips have a conical shape. The probe chip has one cantilever and typical radius of the tip is approximately 10 nm and the cone angle is 40°. Tip height varies between 20-25 µm. According to manufacturer's specifications, resonant frequency varies from 50 kHz to 113 kHz and force constant between 0.17 - 1.7 N/m (suitable for soft materials in tapping mode). Silicon surface has a native oxide layer which makes the probe nonconducting .

CSC38 - contact mode

These are also n-type silicon probes manufactured by MikroMasch. They are used for contact mode. Typical radius and the cone angle are the same as in 19 series.

Tip heigh varies between 20-25 µm. CSC38 contains 3 cantilevers with different lengths (250 µm, 300 µm and 350 µm). Resonant frequency varies between 10-20 kHz and force constant varies from 0.03 to 0.08 N/m (low force constant suitable for contact mode imaging) depending on the length of the cantilever.

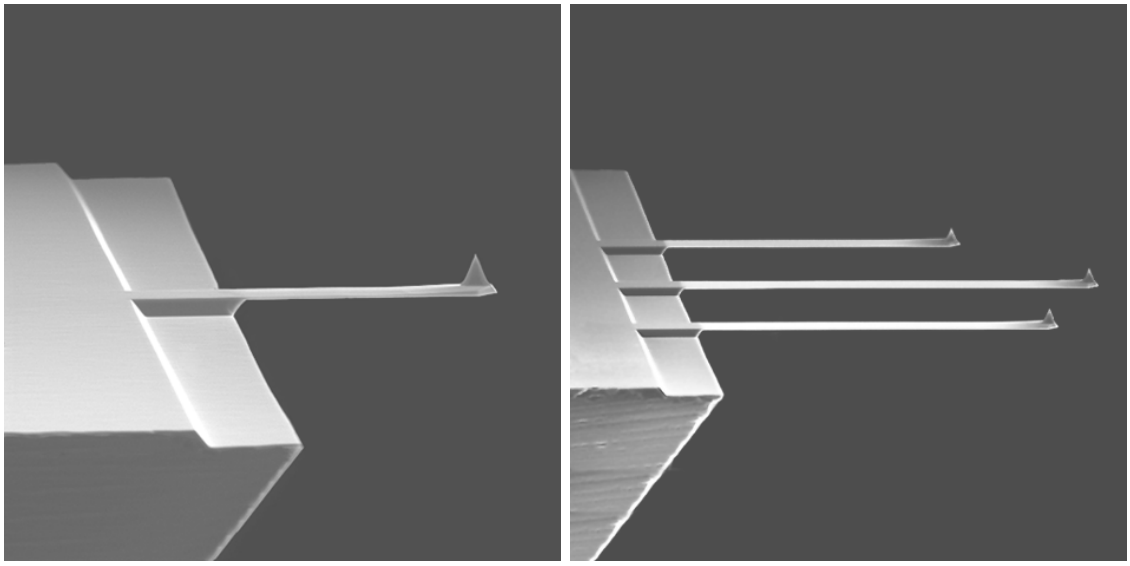

Figure 24. NSC10 series cantilever on the left and CSC38 series on the right. Compared to 19 series, 38 series contains three levers with different lengths so the resonance frequency and spring constant are varying. Images are courtesy of MikroMasch.

AdvancedTEC™ Cont

Third kind of probes, AdvancedTEC™ Cont, were manufactured by Nanosensors™ (Neuchatel, Switzerland). In this model the tip is visible when looking from the top and the radius is less than 10 nanometers. From the figure 25 is seen that the shape of the tip is a bit different than in usual AFM tips. The height of the tip is between 15-20 µm and the cantilever is made from monolithic silicon. According to technical specifications spring constant is 0.2 N/m and resonant frequency is 15 kHz.

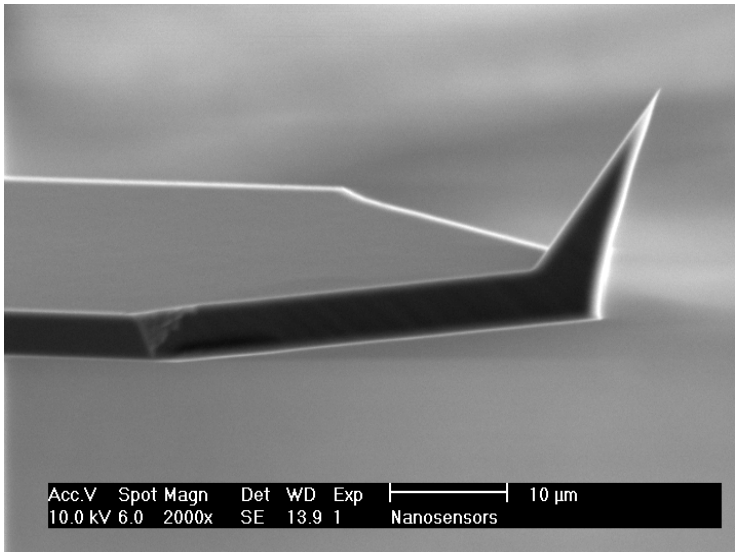

Figure 25. SEM image of the AdvancedTEC tip. From the image is seen that the tip is not perpendicular with the cantilever, which makes it visible from the top and below. Image is courtesy of Nanosensors™.

5.4 Modifications

5.4.1 Hardware

In order to acquire images simultaneously with fluorescence and atomic force microscope, a combination of these two had to be developed. Leica does not have a stage where AFM could be inserted. To install QuickSlide Series 5500 mechanical stage (Agilent Technologies Inc., USA), which was designed to fit in Zeiss Axio Observer D1 microscope (Göttingen, Germany), modifications had to be done. After contacting both manufacturers, Agilent provided technical blueprints for the QuickSlide Series 5500 mechanical stage. Since this stage did not fit straight to Leica TCS SP5, 2 adapter pieces had to be made. After careful measuring 2 adapter pieces from 4 mm thick steel were made. Thickness of 4 mm was chosen since it provided enought space for the objectives to move and focus in z-direction including oil objective. With these adapter pieces QuickSlide Series 5500 mechanical stage fit nicely in to Leica TCS SP5. Design and technical data for these adapter pieces are presented in the appendix.

Space between the condenser and stage was not sufficient for the AFM to fit. In order to create more space, few components from the Leica microscope were detached including 1 detector and condenser lens. This provided more space in z-direction.

5.4.2 AFM probe

Tips from the AFM probes can be detected in the confocal microscope taking advantage of the reflection or autofluorescence. To reach more precise method to pinpoint the tip position, tips were covered with different fluorescent labels. 5 different labels were used with several kind of solvents.

First tips were washed with ethanol (approximately 500 µL) in a small beaker. After drying, 5 µL of fluorescent label was added to the tip. Fluorescent labels were solved in 500 µL of several solvents: ethanol, methanol, dimethyl sulfoxide (DMSO), dimethylformamide (DMF) and chloroform ($CHCl_3$). Used concentrations are presented in the table II.

Aminofunctionalization of the AFM cantilever was also done to make the fluorescent molecules attach more firmly to the tip. For this, different kind of methods have been invented one being gas-phase silanization with aminopropyl-triethoxysilane (APTES) [88]. Tips were first washed in $CHCl_3$ (3 x 5 min) and a desiccator was flooded with nitrogen gas for 3-4 min. Tips were placed inside the nitrogen filled desiccator on a clean surface along with 2 Eppendorf caps other containing 10 µL of triethylamine and the other one 30 µL of APTES were placed inside the desiccator before it was closed. After 120 min of incubation, APTES and triethylamine were removed, the desiccator was flooded with nitrogen gas for 5 min and the tips were left inside for 2 days in order to "cure" the APTES coating [89, 90].

After aminofunctionalization, tips were labelled with fluorescent dye. The dye solution contained 0.24 mg of Atto465 N-Hydroxysuccinimide (NHS) ester and 120

µL of DMF. This was diluted in phosphate buffer (pH 7.2). The diluting ratio was 1:1 total amount being 60 µL. Tips were washed twice in phosphate buffer and then 3 µL of the dye solution was added to each tip. Then they were left in constant shaking for 2 hours. After this tips were washed twice with phosphate buffer and twice with ethanol.

6 Results

6.1 AFM tip

6.1.1 Tip detection

Overlaying can be done when both images have something on them that can be distinguished clearly in both microscopes. These reference points can be fluorescent beads of known size or tip positions of the cantilever. The tip position in the confocal microscope can be detected with reflection or fluorescence. The reflection method proved to be stable but pinpointing the actual position of the tip from these images in nanoscale was hard (see fig. 26). The shape of the reflection PSF is not Gaussian shaped because the tip is a bit tilted and this is a problem when trying to filter the reflection spot to get it smaller. Also it is hard to determine if the signal is reflection, Raman scattering or autofluorescence. Most of the tips gave signal with varying yields of autofluorescence and tip position could be detected in fluorescence image without any coating. The fluorescent coating (examples in fig. 27) improved the yield but it did not attach well to all of the tips and it introduced AFM images to additional convolution.

When tips were detectable in sample plane, AFM tip positions were recorded. AFM software has a built-in feature to move and pinpoint the tip position after the image is scanned. Tip was moved to all four corners in AFM image and this gives the frame for overlaying.

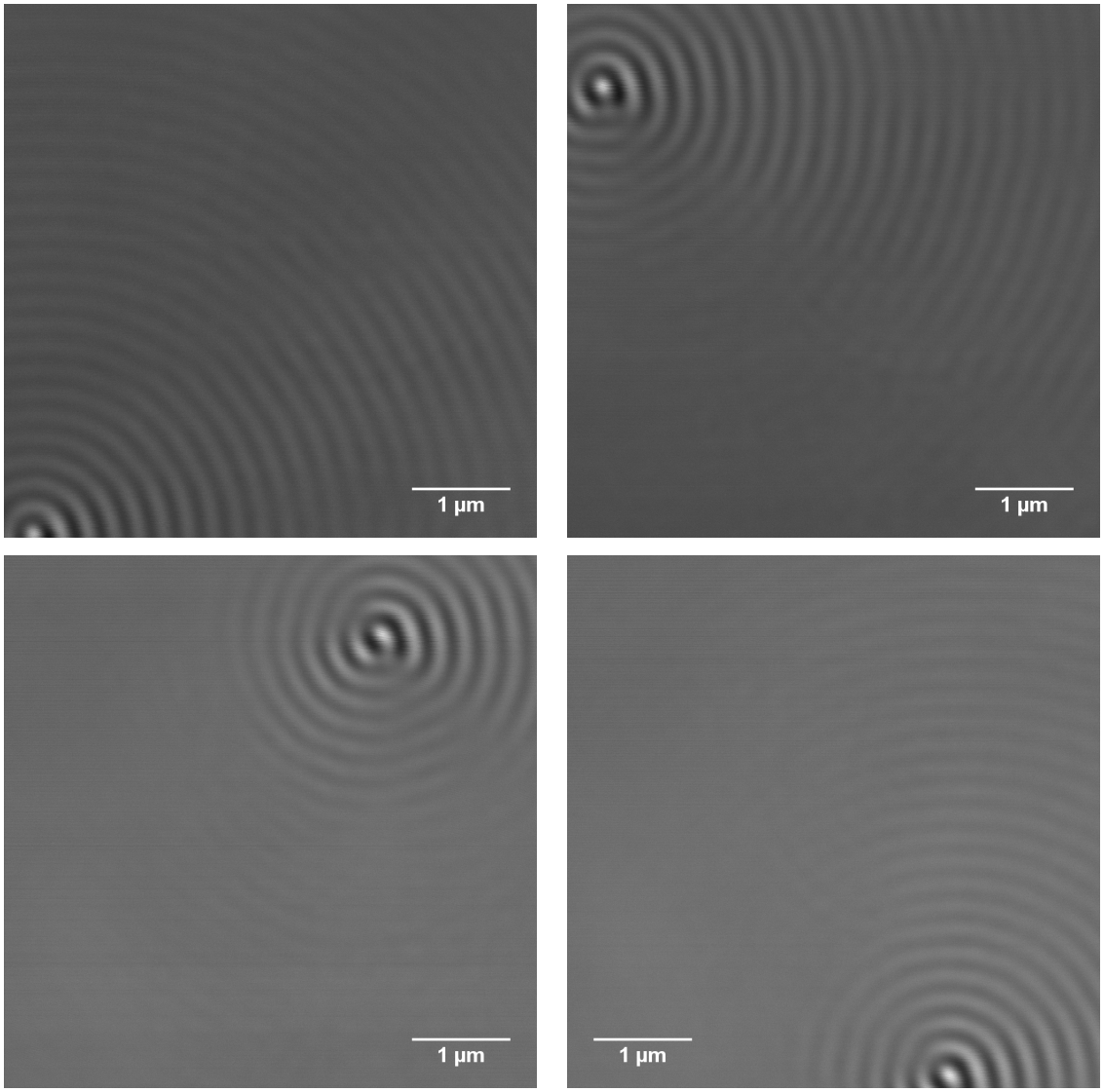

Figure 26. Tip reflection images. The principle is the same as in fluorescence images and tip is moved to four corners and four images are taken to function as a frame for overlaying. Wavelengths used for reflection were 488 nm and 514 nm.

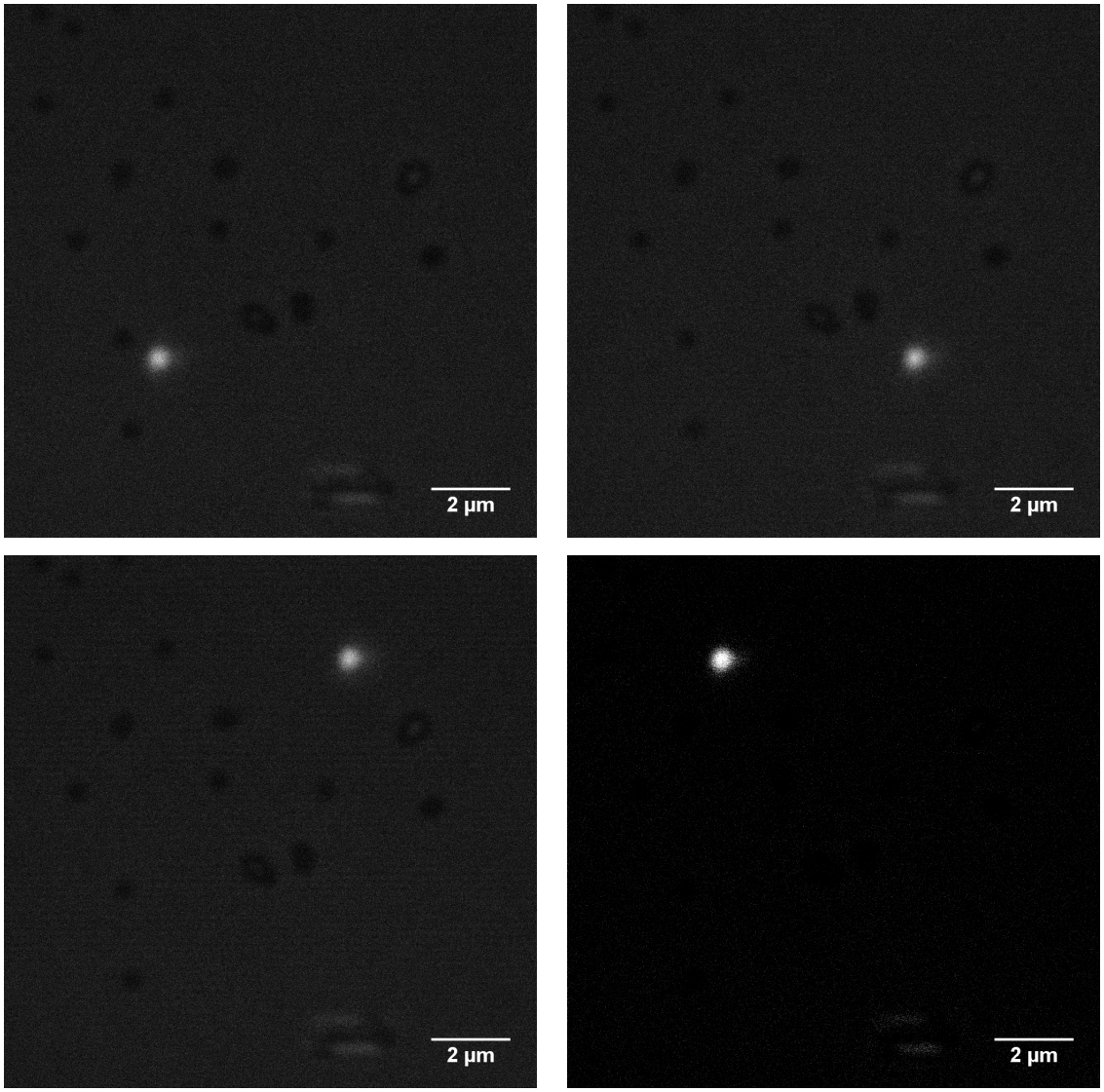

Figure 27. Atto647N coated tip is moved to the corners of the AFM image. This gives the position information which is needed to do the overlay of the images. The dark spots in the images are fluorescent beads that are not fluorescent with the applied wavelength. Tip images are taken with confocal mode and the full width at half maximum (FWHM) is approximately 250-300 nm.

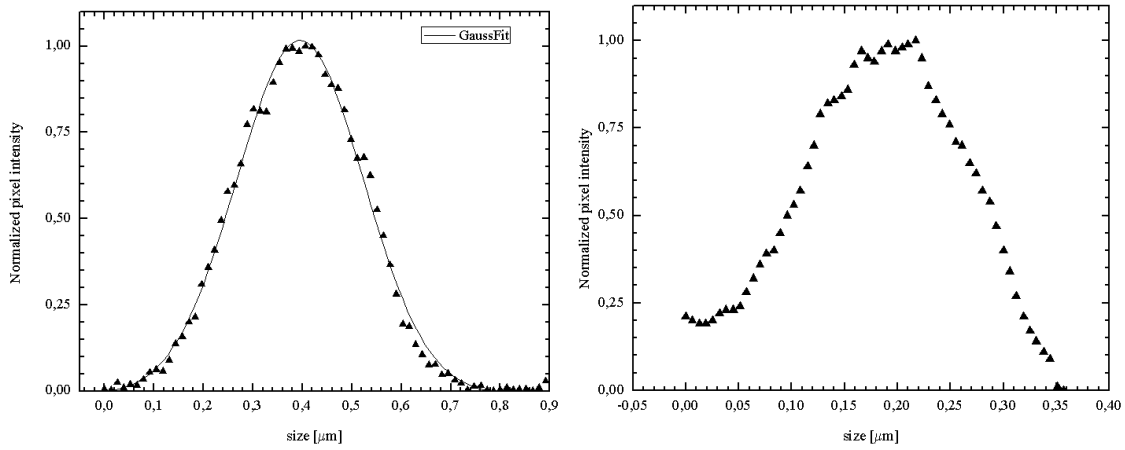

Figure 28. On the left there is fluorescence from the tip plotted with Gaussian fitting and FWHM is approximately 300 nm. On the right there is a graph from tip reflection center and the FWHM is approximately 170 nm.

6.1.2 Tip modifications

Tips were covered with fluorescent material in order to track tip movement and pinpoint its location in confocal fluorescence image. Tip coating methods are described in section 5.4.2. Autofluorescence varied significantly between the tips and in some cases it was good enough to provide information about tip position.

The best fluorescence yield was in Atto647N covered tips. Tip was fluorescent in sample plane with diameter of approximately 600 nanometers when using water objective. The second best tip was 6-(7-Nitro-2,1,3-benzoxadiazol-4-ylamino)hexanoic acid (NiBA) diluted in chloroform but the fluorescence was moderate compared to Atto647N dye. Comparison of these two are presented in figure 29. The fluorescence was weak with 4-(4-Diethylaminostyryl)-1-methylpyridinium iodide (4-Di-2-ASP) dissolved either in chloroform or DMF but it was still visible in sample plane. When testing coated tips it was seen that coating protocol reduced the sum signal in AFM. Due to this reason tips coated rhodamine and 4-Di-2-ASP (diluted with chloroform) could not be used. Used labels and solvents are presented in table II among with their concentrations.

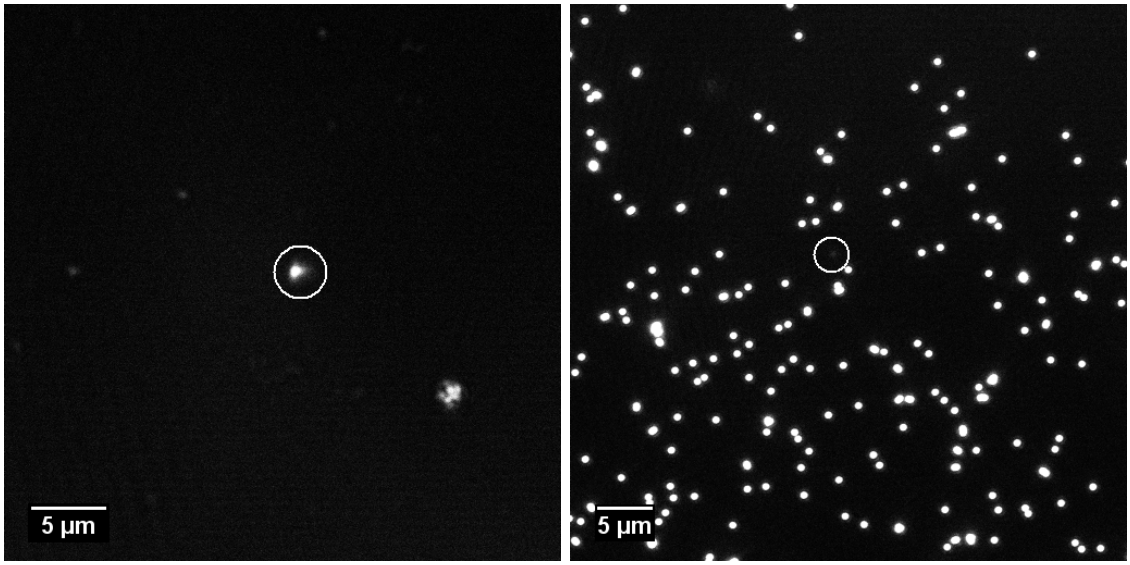

Figure 29. On left Atto647N (dissolved in DMF) was used. Tip (circled) is clearly visible in the sample plane with fluorescent beads. On the right there is NiBA dissolved in chloroform. Fluorescence from the tip (circled) is clearly lower but still visible in sample plane.

Table II. Used labels, solvents and their concentrations. All dyes were dissolved in 500 µL of solvent. 4-Di-2-ASP = 4-(4-Diethylaminostyryl)-1-methylpyridinium iodide and NiBA = 6-(7-Nitro-2,1,3-benzoxadiazol-4-ylamino)hexanoic acid.

Label	Solvent	ρ (mg/µL)	Label	Solvent	ρ (mg/µL)
Rhodamine	Ethanol	$3.7 \cdot 10^{-8}$	NiBA	DMSO	$1.6 \cdot 10^{-3}$
Atto647N	Ethanol	-	NiBA	$CHCl_3$	$1.4 \cdot 10^{-3}$
DCM	Ethanol	$5.4 \cdot 10^{-3}$	4-Di-2-ASP	Methanol	$1.2 \cdot 10^{-3}$
DCM	DMSO	$1.6 \cdot 10^{-3}$	4-Di-2-ASP	DMSO	$1.3 \cdot 10^{-3}$
4-Di-2-ASP	DMF	$2.3 \cdot 10^{-3}$	4-Di-2-ASP	$CHCl_3$	$1.4 \cdot 10^{-3}$
NiBA	Methanol	$3.1 \cdot 10^{-3}$	NiBA	DMF	$1.2 \cdot 10^{-3}$

6.2 Samples

6.2.1 Nanodiamond samples

Single nanodiamonds were hard to detect since they were clustered quite tightly even after sonication procedures. Fluorescence originates from silicon- or nitrogen-vacancies in the diamond structure. Some of the ND samples had good fluorescence

but mostly it was moderate. The biggest concern was that only a fraction of NDs were fluorescent. After scanning the area with AFM (see fig. 30), it was clear that nanodiamonds were not good reference points for overlaying, because lots of the diamonds did not emit any fluorescence at all. Total of 6 different ND samples were tested multiple times with several different dilution ratios (see table I for ratios). It was clear that these provided samples were not good to use as reference particles or fluorescent probes, since the only a small portion of the sample NDs were fluorescent.

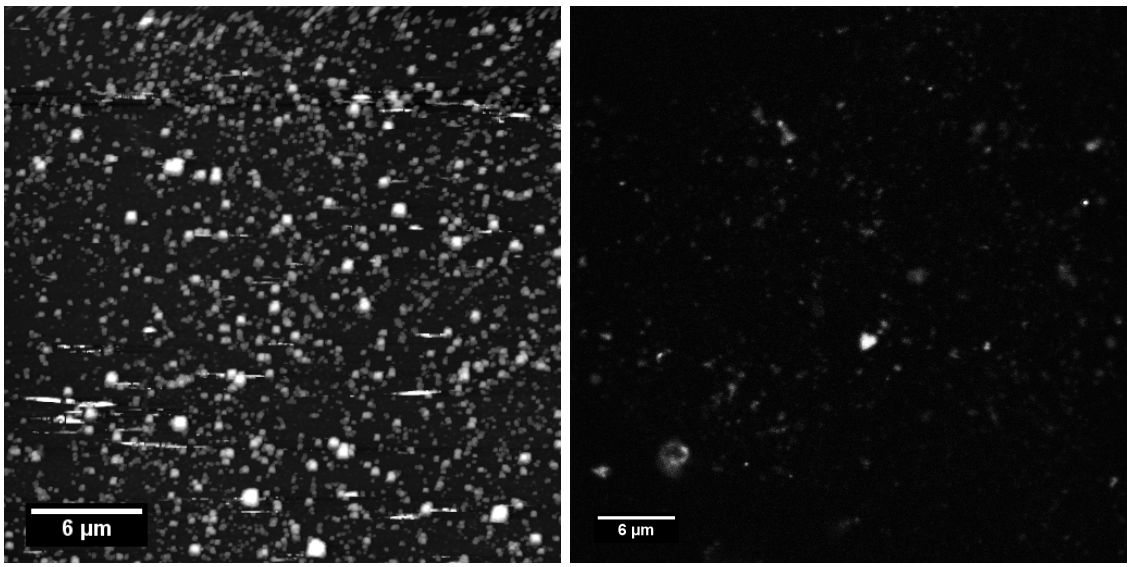

Figure 30. Fluorescence image acquired from the ND4 sample is presented on the right. Sample was diluted in ethanol with ratio 1:100 and excitation wavelength of 488 nm was used with a image size of 45 µm × 45 µm. The diameter of biggest clusters are approximately 1 µm, smallest ones being approximately 150 nm. On the left there is AFM image acquired from one prepared ND sample, which was also diluted in ethanol with ratio 1:100. Scan size of the AFM image is 30 µm × 30 µm. It is easily seen from the picture that ND concentration is high but very few NDs are actually fluorescent (around 10 %).

6.2.2 Quantum dots

Quantum dots are luminescent nanoparticles and the size of the crystal determines most of the characteristics of the Qdot. The physical reason for this is the quantum confinement effect which breaks the band gap into quantized energy levels when particle size is smaller than Bohr exciton radius. Absorption of a photon with energy above the semiconductor band gap energy results in the creation of an electron-

hole pair (or exciton). All Qdots have wide absorption spectra and they are easily excitable with ultraviolet light. Smaller Qdots emit fluorescence in blue range (high energy) and larger Qdots emit fluorescence in red region (low energy). Emission peaks are narrow and symmetric because the transitions in energy levels are not coupled with atomic vibrations [91].

In test samples single Qdots were hard to detect since fluorescence signal was weak when trying to pinpoint individual dots and this was due to our excitation wavelength (shortest wavelength being 458 nm with Argon laser). Although clusters of Qdots emitted really bright fluorescence (see fig. 31). Potential toxicity of Qdots probes in vivo imaging still remains an issue so whether they are suitable to use as reference particles in osteoclast imaging is still unknown [92].

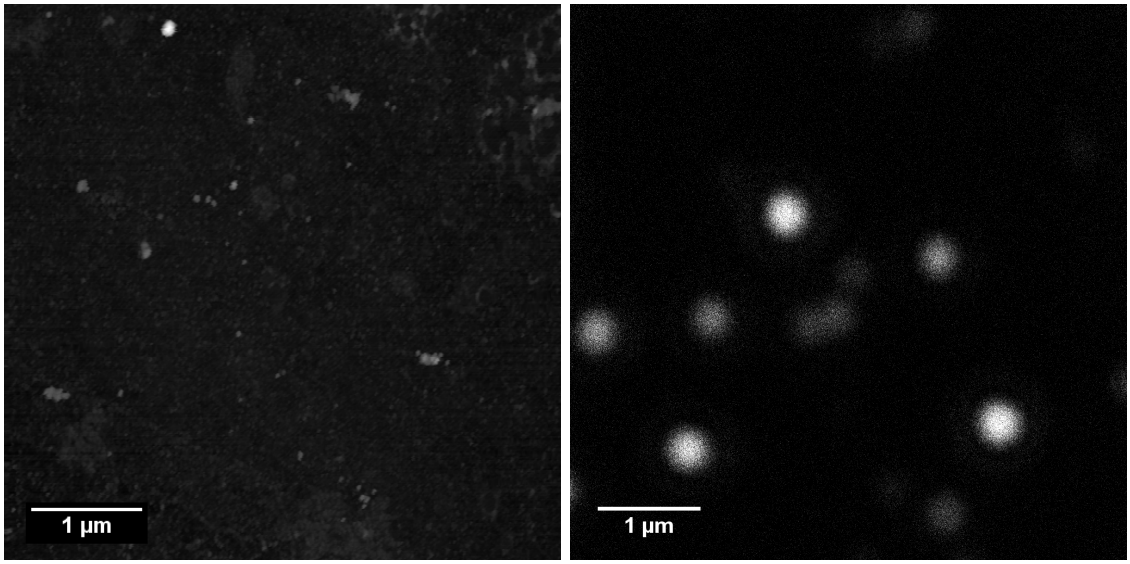

Figure 31. Quantum dot clusters (cluster size varied from 50-100 nm) were emitting really bright fluorescence which can be seen on the right. The FWHM was approximately 300 nm and the scan size for AFM image was 5 µm × 5 µm and for the fluorescence image 5.41 µm × 5.41 µm. It is seen that the individual Qdots are not seen in the fluorescence image for some reason.

6.2.3 Carboxy-modified microspheres

Fluospheres® fluorescent beads have pendent carboxylic acids, making them suitable for covalent coupling of proteins and other amine-containing biomolecules using water-soluble carbodiimide reagents. The diameter of the spheres is 170 nm and the

absorption peak is at 540 nm and they emit orange fluorescence ($\lambda_{peak} = 560$ nm). Microspheres were excited with 514 nm (CW Argon laser) and they emitted bright fluorescence as seen in the figure 32. The size of the fluorescence spots were between 200-300 nm with normal confocal imaging mode. The beads were separated quite nicely and they did not bleach easily. Also the fluorescence was emitted point-like and did not spread (sharp PSF).

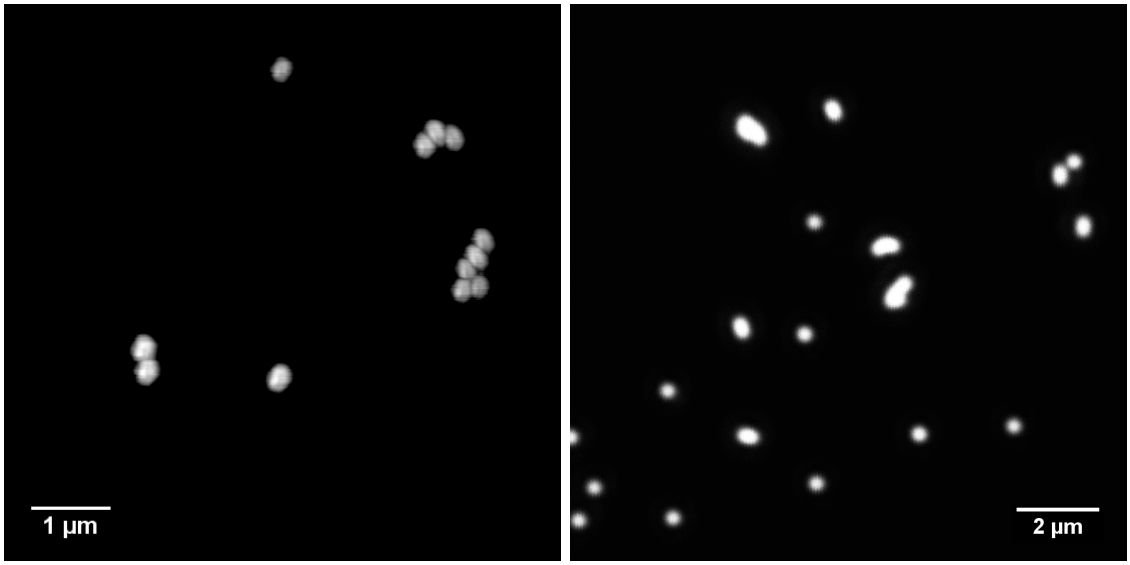

Figure 32. On the left AFM topography trace image from microspheres (scanning size 7 µm × 7 µm). On the right there is a fluorescence image from the same area with image size 13.41 µm × 13.41 µm. The FWHM of the fluorescence spot was approximately 300 nm with confocal setup.

6.2.4 Osteoclasts

Labeling of the osteoclasts was good and several osteoclasts with multiple nuclei were found in the samples. Earlier time points were better since in the later ones cells were already in apoptosis. In figure 34 there is an example images from a multinuclei cell.

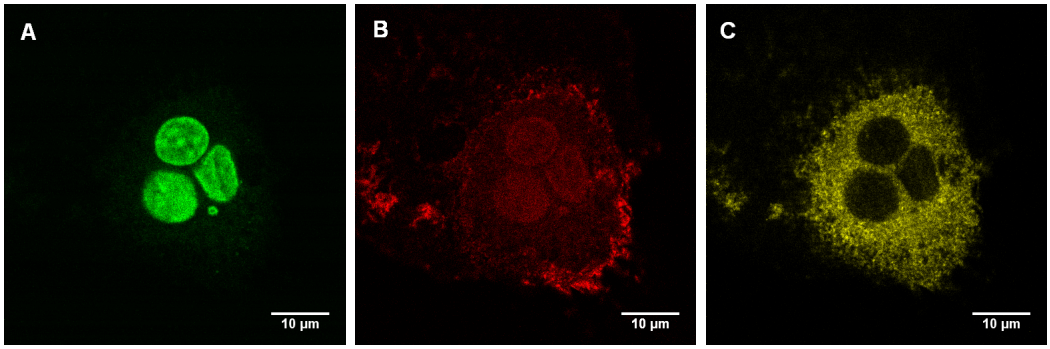

Figure 33. Channel A is detecting emission from nuclei staining ($\lambda_{exc} = 488$ nm) and 3 separate nuclei are seen. Channel B is detecting emission from Chromeo494 ($\lambda_{exc} = 496$ nm) labelled integrin and channel C is detecting emission from tyrosine kinase labelled with Atto647N ($\lambda_{exc} = 633$ nm). Saturation is modified in all images to make images a bit brighter.

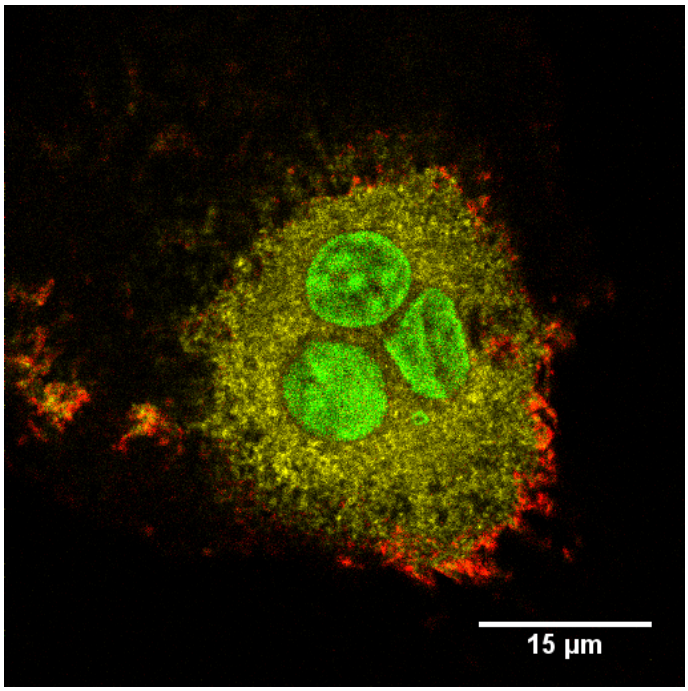

Figure 34. Images in figure 33 combined. Osteoclast was activated with milled bovine bone particles and fixed after 1 hour from the exposure. There is co-localization of c-Src and $\alpha_V\beta_3$ and this indicates that the cell is active and signalling. Image was taken in confocal mode with water objective (HCX PL APO CS 63.0x 1.20 WATER UV).

Osteoclast imaging with AFM proved to be a difficult task since they are really soft and delicate. During experiments several cells were destroyed when AFM tip poked holes into them and the cells also got stuck to the tip and this broke the membrane of the cell releasing the cytosol. In the figure 36 there is a decent AFM

image from the edge of the osteoclast. No proper overlay could be done since tip position images were bad since the fluorescence spots were not point-like.

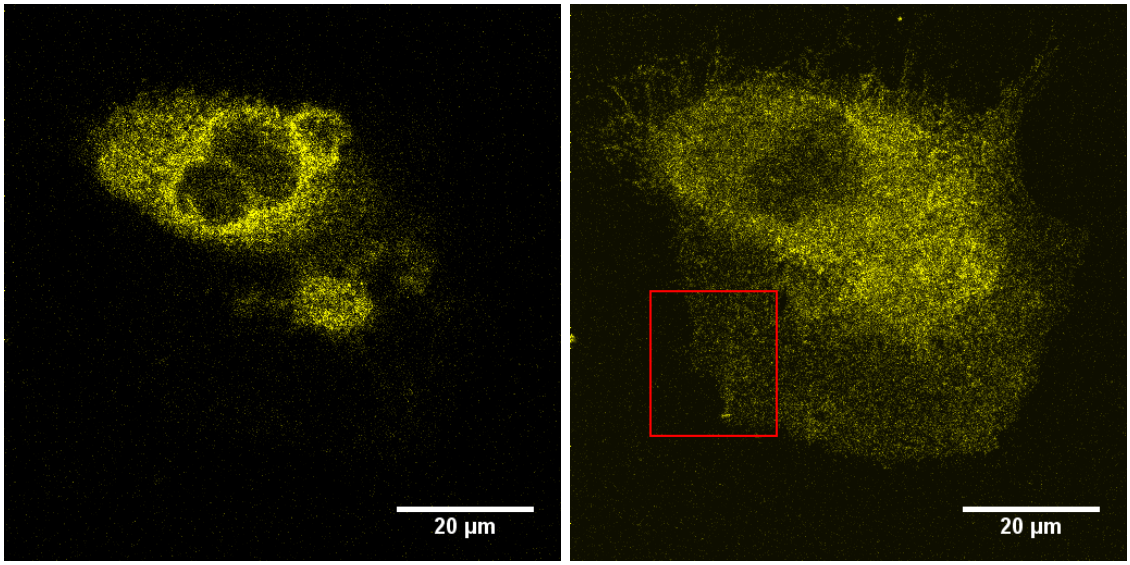

Figure 35. Osteoclast imaging. Both images are from the same cell but from slightly different z-planes. The left image is further away from the surface and several nuclei can be clearly seen in the osteoclast. The right image is closer to the cover slip and attachment to the cover slip is seen. This channel was detecting c-Src labelled with Atto647N. Used image size was 80.98 × 80.98 µm.

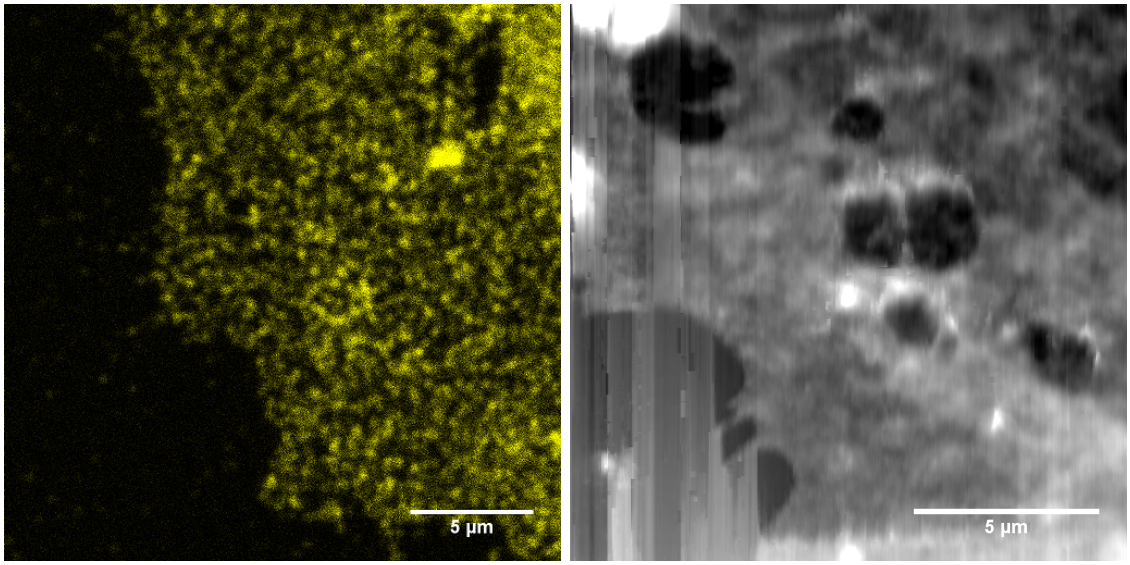

Figure 36. Same area imaged with AFM and fluorescence microscope. AFM frame is not entirely perfect due to difficulties in non-contact imaging. Setpoint had to be kept really low to have a soft contact and this resulted frequent contact losses (tip got too far away from attractive regime). The area in the image is same which is highlighted in figure 35 with a red square. The exact image size for fluorescent image was 20.63 µm × 20.63 µm and for topography trace image 15 µm × 15 µm. AFM image was taken in non-contact mode with a scanning speed between 7.5-15 µm/s.

6.3 Data processing

6.3.1 ImageJ

ImageJ is an image processing and analysis software based on Java programming language. User-written plugins and recordable macros make it a versatile tool in life science studies. It has a wide range of filters and since it is a free-ware, various macros and plugins for different kind of purposes are available. Plugins are addons that are written using Java programming language and they expand the functionality of ImageJ [93]. For our experiment we used a plugin called TurboReg [94]. This plugin is designed to align images using landmarks that can be chosen manually or automatically. Landmarks are chosen from source image and also from target image. Then plugin will modify the source image to match dimensions of the target image.

6.3.2 Used macro

Macros can be easily recorded with ImageJ macro recorder. Basically the macro executes different tasks in ImageJ and automates the image processing procedure. This ensures that the images are always processed in the same way and user does not have to remember everything. Since processing is automated with a macro, it is fast and it discards errors made by user. Furthermore it enables user to process batches of images and it can be combined with microscope software to process the images in real time. This macro is explained as flowchart in figure 37 and below there is a detailed explanation what the macro does:

1. Before doing any image processing, macro defines default values for filtering settings so that tip position extraction is automated. These default values are obtained by testing with sample images and finding proper values.

2. The macro closes all windows that are open and gives introduction screen for the user which includes the instructions what is about to happen.

3. Fluorescence images from AFM tip positions are opened next to serve as landmarks. Depending from the user, 3 to 4 images are opened. These images are automatically organized on the screen and resized depending on how many images have been opened. If user selects less than 3 images, error dialogue will appear and macro will close itself.

4. After selecting sufficient number of images, macro will create arrays for x- and y-coordinates.

5. Tip images are processed with filters to acquire the tip position. Macro uses median filter and after that find maxima -function. Coordinates from these tip positions are saved to the arrays.

6. If there is zero or more than one maxima in one image, macro will ask user to manually set threshold minimum and maximum values. Cancelling this will execute close all -command. After this x- and y-coordinates are saved from different tip images to their own arrays.

7. Coordinates are sorted since there is no particular way to select the tip images for landmarks e.g. with three images, selection can be made in four different ways.

8. Landmarks for the overlaying are now acquired. Next macro will ask for the AFM image and after selecting the desired image, macro filters the noise. AFM image will be adjusted according to landmarks.

9. STED fluorescence image selection is next.

10. Overlaying is done with TurboReg plugin.

11. Final image is cleaned up with filters.

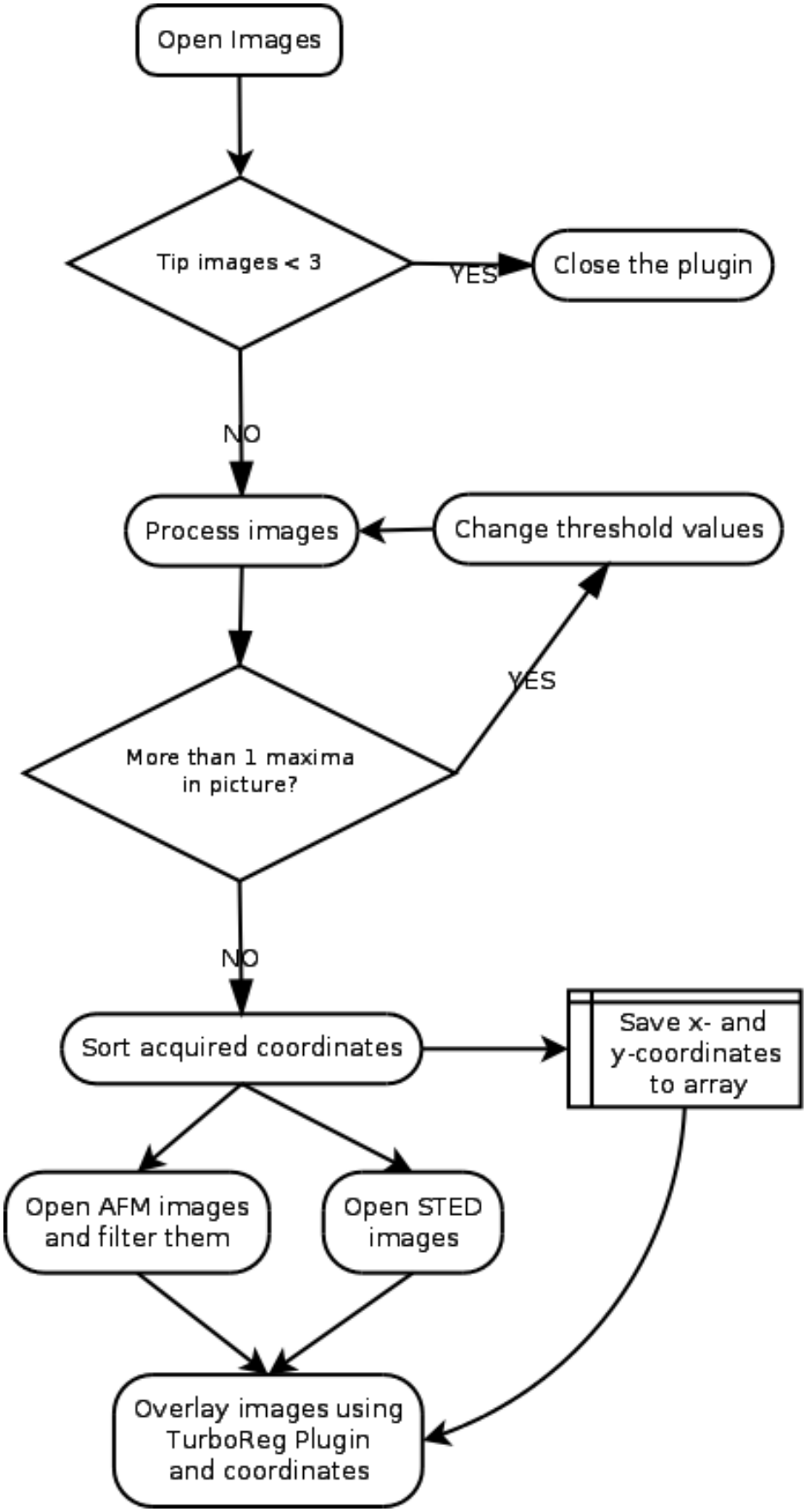

Figure 37. A flowchart of the macro.

6.3.3 Combining images

After fluorescence images of the tip from all four corners have been acquired, fluorescence image of the sample was taken. Tip positions from the corners give a frame for the x- and y-dimensions for the fluorescence image. AFM topography image was taken first due to long scanning time.

Once these three images are acquired (tip positions, fluorescence image and topography image) overlaying can be done. Topography image can be a bit tilted in lateral direction when lookin the tip positions in fluorescence image so straightforward overlaying is difficult. TurboReg-plugin utilizes 1-4 landmarks depending on the situation. These landmarks are positioned in the corners of the topography image and on top of the fluorescent tip positions in fluorescence image. Additionally reference beads can be used as landmarks when imaging samples. The reason to use tip positions and reference beads is simple. When doing the overlaying, it is better not to use the actual data for overlaying. If the actual data is used, then the overlay image can be compromised and the fluorescence that is seen in the image, might not come from that actual spot.

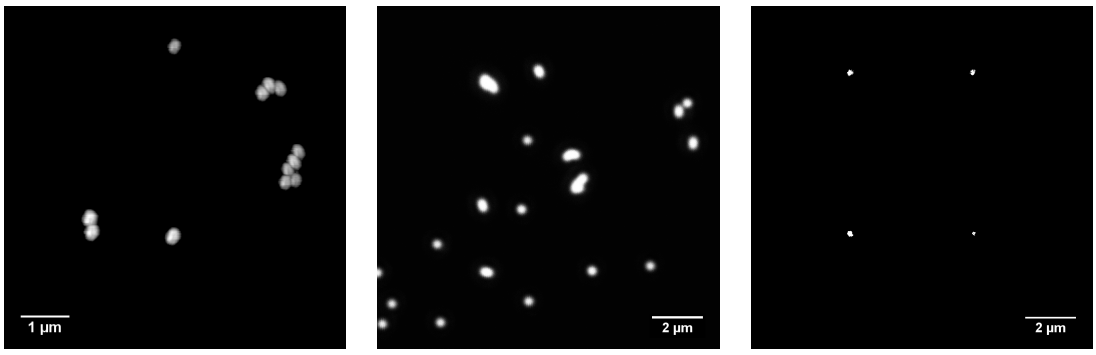

Figure 38. Before doing overlay with tip positions three images should be ready: 1) topography image of the sample 2) fluorescence image of the sample and 3) fluorescence image of the tips. All images should be processed individually and then combined.

6.4 Overlaying

The first overlaying images were done with the confocal setup so the resolution was limited to approximately 200 nm. The tip position images were filtered with mean filter to get a more accurate position of the fluorescence center. Mean and median filters were used to filter the tip images. To visualize better the overlaying, fluorescence is seen as blue and fluorescent beads imaged with AFM are in grey scale image. The offset was measured from the final images and it was approximately 50 nm in the first images.

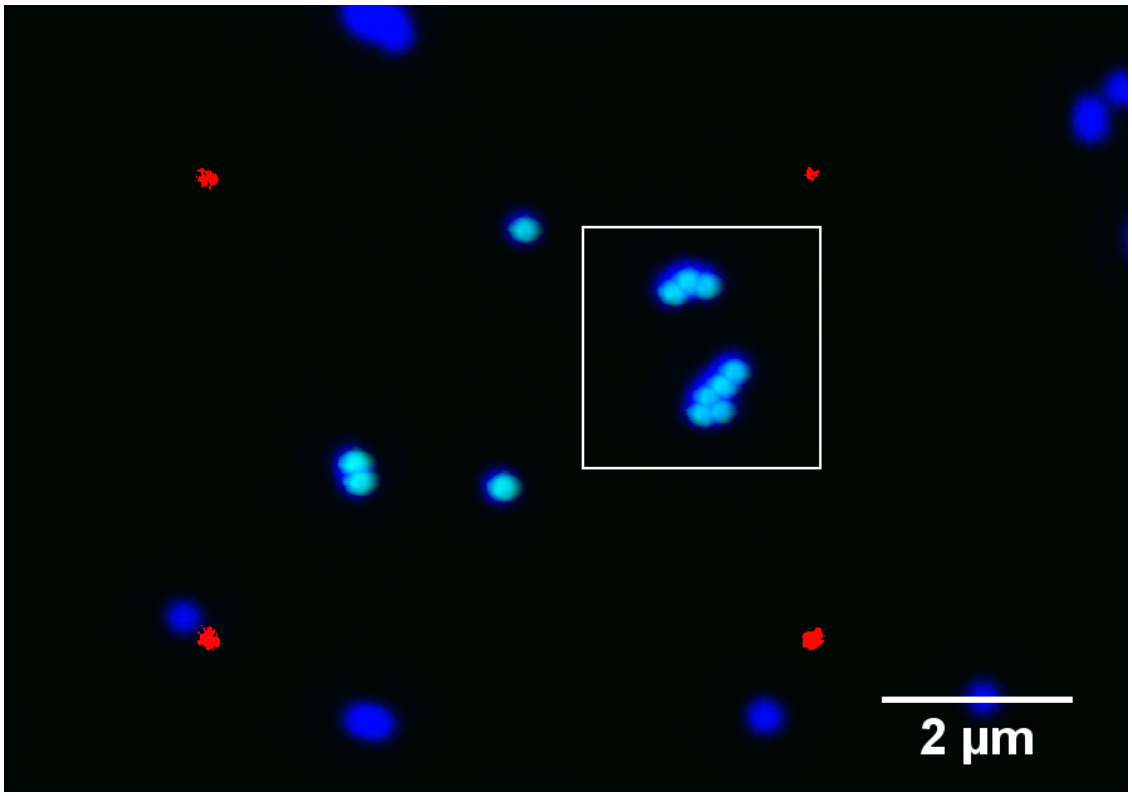

Figure 39. The final image after overlaying. The red dots represent the tip positions, blue is fluorescence from the beads. Combined images are the same images as seen in figure 32. Fluorescence images are taken with confocal settings so the optical resolution is still more than 200 nm. Images were taken together with Takahiro Deguchi in the laboratory of Biophysics.

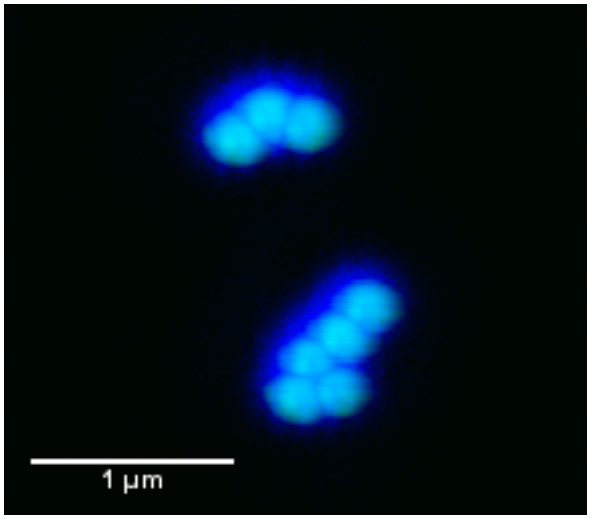

Figure 40. Squared are from the figure 39. Pixels are visible but this is just to demonstrate how well the overlaying succeeded.

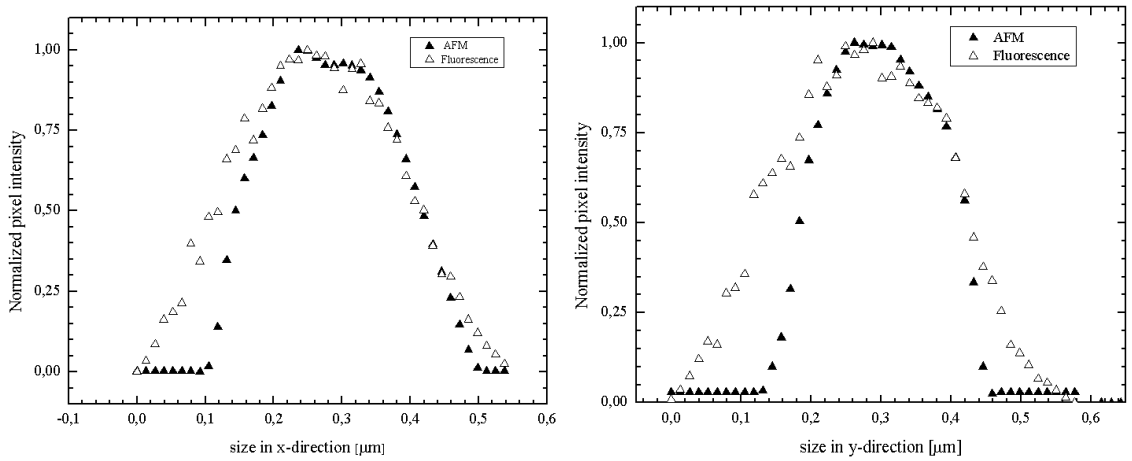

Figure 41. Pixel intensity profiles taken from x- and y-axis. Fluorescence is coming only from the beads. Size of the beads is bit too big and this is due to tip convolution since no deconvolution was done.

Overlaying of osteoclast images that were obtained was difficult since the tip position images were not good. This is because tip was not coated with Atto647N and only autofluorescence from the tip was detected. This resulted in a non-spherical fluorescence spot as seen in the figure 42.

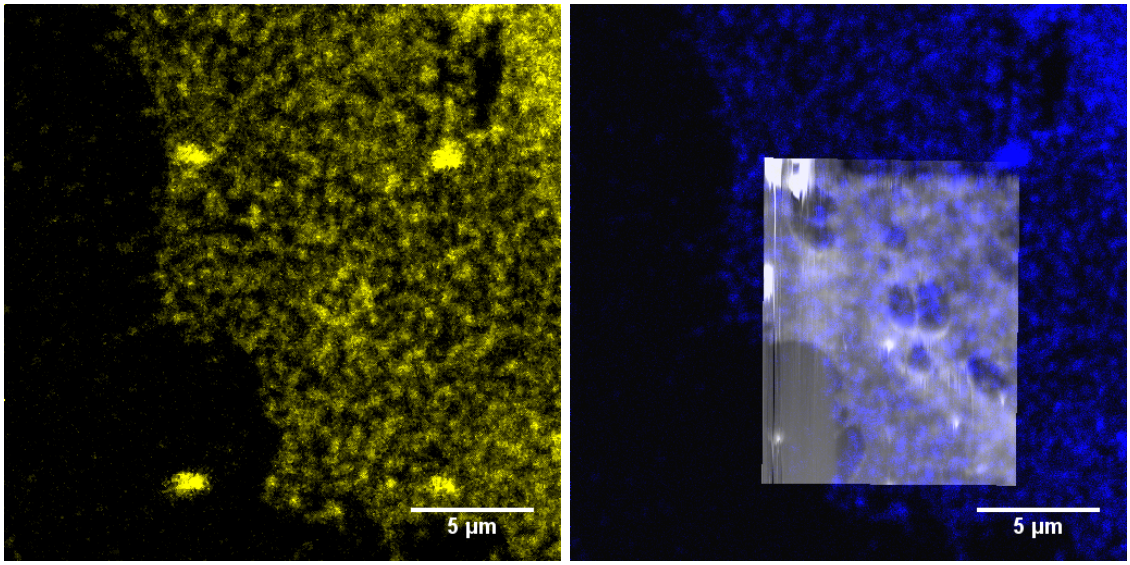

Figure 42. On the left tip positions are seen. Coated tip was not used and it is seen that the tip spots are not symmetrical which makes the tip detection and filtering difficult. On the right there is a overlay of fluorescence and AFM image seen in figure 36. Fluorescence is presented with blue color since with other colors the AFM image had poor visibility.

During image acquisitions there were vibrations seen in fluorescence images and additional noise in AFM images. The cause of this remains unknown but it is most likely caused by the multi-photon cooling system which is located under the optical table. After turning off the cooling, quality of AFM images were better and less noise was seen.

7 Discussion

The high resolution AFM and the optical super-resolution STED microscope were succesfully combined in these experiments. While the old CLSM and AFM combinations already provide this simultaneous imaging technique, optical resolution is still limited by diffraction of the light [95, 96]. With our new system, optical resolution of 50 nm is possible, which is significantly below the diffraction limit. In the experiments we were able to combine fluorescence and AFM images with a slight offset of 50 nm. This kind of offset can be considered to be small since it is approximately the current resolution of our STED microscope. The most likely cause of this offset

is the manual overlaying procedure, where the absolute tip position is still not found precisely enough.

In the development process of our new method, several different test samples were used. It was easily seen that considerable amount of the NDs and Qdots did not emit fluorescence. Because images could be taken precisely from the same spot, this conclusion could be done easily. To address this fluorescence yield problem, new ND samples should be acquired with higher amount of silicon or nitrogen vacancies and for Qdots a suitable excitation laser in ultraviolet range is needed.

Information gathered from the experiments will be useful to further improve the new system and overcome problems we have encountered. Overlaying of some image worked well, but lots of raw data is needed to master the overlaying process. Since the STED microscope is commercial, some problems could only be fixed by Leica's own engineers. Especially beam alignment did not work well, which affected tremendously to the depletion. This is one of the reasons why simultaneous STED image and AFM image was not required. Apart from this, sample movement was an issue. Experiments were performed in ambient conditions and temperature was mainly between 21-23 °C. Even with this temperature fluctuation some sample drifting was experienced. To address this problem, thermoelectric cooling should be used to gain more precise control over the sample temperature and avoid unnecessary drifting. Additionally, even the slightest touch to the optical table or adjustment of the AFM laser (done manually) caused sample to move tens of nanometers.

Further experiments should include manufacturing of calibration samples to easily verify that the overlaying data is correct. These samples should include particles which dimensions are known precisely and they should not aggregate. Also they should not photobleach easily and quantum yield should be high. And when using STED, the particles should be able to be depleted and with our system it means that the emission peak should be towards the red region. Additionally, to further

improve the optical resolution, used sample buffer should have a refractive index close to 1.51 and optical mismatch should be minimal.

During the experiments only few of the AFM imaging modes were used. To fully take advantage of AFM, other imaging modes should be also tested. These modes include PicoTREC imaging and FS. In our experiments more than 20 cantilevers were used; some of them were being coated with fluorescent material. The coating of the tip with fluorescent material had an effect in AFM resolution but to get the tip clearly visible in the sample plane coating was necessary. Autofluorescence yield was fairly good in some cases but the yield varied too much to be stable method for detection. Tips had silicon vacancies which made them fluorescent but this is a byproduct of tip manufacturing process and not an implemented feature.

Since two commercial microscopes were used, experiment included two different control softwares for the microscopes and there was not any communication between them. Several tips were broken in the experiments when objective was raised too much. To prevent this, communication between softawares should be established. Additionally, it would be highly beneficial if the overlaying could be done automatically after imaging and user would have overlaying image without having to use ImageJ for image processing.

This new method brings the optical resolution down to AFM level where it can be utilized properly and it allows data recording from the same spot without moving the sample between image acquisitions. Main applications for this new imaging modality lie in cell biology. A good example from this is osteoclast binding studies. The fluorescence signal tells where the binding has occurred and if it is signaling (active). This determines also if the binding is specific or unspecific. AFM gives the topographical data with normal modes or force of the binding with force spectroscopy. Basically everything can be imaged with our design as long as the fluorescence photons get through the sample.

References

[1] R. A. von Kölliker, *Die normale Resorption der Knochengewebes und ihre Bedeutung für die Entstehung der typischen Knochenformen.* Leipzig: F.C.W. Vogel, 1873.

[2] G. H. Enevoldsen, *Scanning Probe Microscopy Studies of a Metal Oxide Surface - a detailed study of the* TiO_2*(110) surface.* PhD thesis, University of Aarhus, 2007.

[3] P. P. Lehenkari and M. A. Horton, "Single Integrin Molecule Adhesion Forces in Intact Cells Measured by Atomic Force Microscopy," *Biochemical and Biophysical Research Communications*, vol. 259, no. 3, pp. 645 – 650, 1999.

[4] E. Rittweger, K. Y. Han, S. E. Irvine, C. Eggeling, and S. W. Hell, "STED microscopy reveals crystal colour centres with nanometric resolution," *Nature Photon.*, vol. 3, pp. 144–147, February 2009.

[5] W. J. Croft, *Under the Microscope: Brief History of Microscopy*, vol. 5 of *Series in Popular Science.* 5 Toh Tuck Link, Singapore 596224: World Scientific Publishing Co. Pte. Ltd., 2006.

[6] R. Hooke, *Micrographia: or, Some physiological descriptions of minute bodies made by magnifying glasses.* London: J. Martyn and J. Allestry, 1st ed., 1665.

[7] A. van Leeuwenhoek and H. Samuel, *The Selected Works of Antony van Leeuwenhoek Containing His Microscopical Discoveries in Many of the Works of Nature*, vol. 2. London: G. Sidney, 1800.

[8] A. van Leeuwenhoek, *The collected letters from Antoni van Leeuwenhoek*, vol. 2. Amsterdam: Sweets and Zeitlinger LTD, 1941.

[9] O. Eppenstein and S. Czapski, *Grundzüge der Theorie der optischen Instrumente nach Abbe.* Leipzig: J. A. Barth, 1904.

[10] E. Abbe, "Beiträge zur theorie des mikroskops und der mikroskopischen wahrnehmung," *Archiv für Mikroskopische Anatomie*, vol. 9, no. 1, pp. 413–418, 1873.

[11] A. Köhler, "Gedanken zu einem neuen Belechtungsverfahren für mikrophotographische Zwecke," *Zeitschrift für wissenschaftliche Mikroskopie*, 1893.

[12] F. Zernike, "Phase contrast, a new method for the microscopic observation of transparent objects part I," *Physica*, vol. 9, no. 10, pp. 686–698, 1942.

[13] D. B. Murphy, *Fundamentals of light microscopy and electronic imaging.* New York: Wiley-Liss, 2001.

[14] M. Knoll, "Aufladepotentiel und Sekundäremission elektronenbestrahlter Körper," *Zeitschrift für technische Physik*, vol. 16, pp. 467–475, 1935.

[15] M. von Ardenne, "Das elektronen-rastermikroskop," *Zeitschrift für Physik*, vol. 109, no. 9, pp. 553–572, 1938.

[16] G. Binnig and H. Rohrer, "Scanning tunneling microscopy," *IBM J. Res. Dev.*, vol. 30, pp. 355–369, July 1986.

[17] G. Binnig, C. F. Quate, and C. Gerber, "Atomic force microscope," *Phys. Rev. Lett.*, vol. 56, pp. 930–933, Mar. 1986.

[18] W. Denk, J. H. Strickler, and W. Webb, "Two-photon laser scanning fluorescence microscopy," *Science*, vol. 248, no. 4951, pp. 73–76, 1990.

[19] S. Hell and E. H. K. Stelzer, "Properties of a 4Pi confocal fluorescence microscope," *J. Opt. Soc. Am. A*, vol. 9, pp. 2159–2166, Dec. 1992.

[20] S. W. Hell, E. H. K. Stelzer, S. Lindek, and C. Cremer, "Confocal microscopy with an increased detection aperture: type-B 4Pi confocal microscopy," *Opt. Lett.*, vol. 19, pp. 222–224, Feb. 1994.

[21] E. H. K. Stelzer and S. Lindek, "Fundamental reduction of the observation volume in far-field light microscopy by detection orthogonal to the illumination axis: confocal theta microscopy," *Opt. Commun.*, vol. 111, no. 5-6, pp. 536–547, 1994.

[22] S. W. Hell and J. Wichmann, "Breaking the diffraction resolution limit by stimulated emission: stimulated-emission-depletion fluorescence microscopy," *Opt. Lett.*, vol. 19, pp. 780–782, June 1994.

[23] E. Betzig, G. H. Patterson, R. Sougrat, O. W. Lindwasser, S. Olenych, J. S. Bonifacino, M. W. Davidson, J. Lippincott-Schwartz, and H. F. Hess, "Imaging Intracellular Fluorescent Proteins at Nanometer Resolution," *Science*, vol. 313, no. 5793, pp. 1642–1645, 2006.

[24] M. J. Rust, M. Bates, and X. Zhuang, "Sub-diffraction-limit imaging by stochastic optical reconstruction microscopy (STORM)," *Nat. Methods*, vol. 3, no. 10, pp. 793–795, 2006.

[25] R. C. Dunn, "Near-field scanning optical microscopy," *Chem. Rev.*, vol. 99, no. 10, pp. 2891–2928, 1999.

[26] K. C. Neuman and A. Nagy, "Single-molecule force spectroscopy: optical tweezers, magnetic tweezers and atomic force microscopy," 2008.

[27] T. A. Sulchek, R. W. Friddle, K. Langry, E. Y. Lau, H. Albrecht, T. V. Ratto, S. J. DeNardo, M. E. Colvin, and A. Noy, "Dynamic force spectroscopy of parallel individual mucin1-antibody bonds," *PNAS*, vol. 102, no. 46, pp. 16638–16643, 2005.

[28] Y. L. Lyubchenko and L. S. Shlyakhtenko, "AFM for analysis of structure and dynamics of DNA and protein-DNA complexes," *Methods*, vol. 47, no. 3, pp. 206–213, 2009.

[29] Y. Wu, J. Cai, L. Cheng, C. Wang, and Y. Chen, "Chromosome imaging by atomic force microscopy: influencing factors and comparative evaluation," *Journal of Genetics*, vol. 85, no. 2, pp. 141–145, 2006.

[30] M. A. Hussain, A. Agnihotri, and C. A. Siedlecki, "AFM Imaging of Ligand Binding to Platelet Integrin $\alpha_{\|b}\beta_3$ Receptors Reconstituted into Planar Lipid Bilayers," *Langmuir*, vol. 21, no. 15, pp. 6979–6986, 2005.

[31] F. Kienberger, A. Ebner, H. J. Gruber, and P. Hinterdorfer, "Molecular Recognition Imaging and Force Spectroscopy of Single Biomolecules," *Accounts of Chemical Research*, vol. 39, no. 1, pp. 29–36, 2006.

[32] P. Hinterdorfer and Y. F. Dufrene, "Detection and localization of single molecular recognition events using atomic force microscopy," *Nat. Methods*, vol. 3, pp. 347–355, May 2006.

[33] M. Todorovic and S. Schultz, "Magnetic force microscopy using nonoptical piezoelectric quartz tuning fork detection design with applications to magnetic recording studies," *J. Appl. Phys.*, vol. 83, no. 11, pp. 6229–6231, 1998.

[34] D. Xu, G. D. Watt, J. N. Harb, and R. C. Davis, "Electrical conductivity of ferritin proteins by conductive AFM," *Nano Letters*, vol. 5, no. 4, pp. 571–577, 2005.

[35] G. Lippmann, "Principe de la conservation de l'électricité, ou second principe de la théorie des phénomènes électriques," *J. Phys. Theor. Appl.*, vol. 10, no. 1, pp. 381–394, 1881.

[36] B. Bhikkaji, M. Ratnam, and S. Moheimani, "PVPF control of piezoelectric tube scanners," *Sensors and Actuators A: Physical*, vol. 135, no. 2, pp. 700–712, 2007.

[37] "Cantilevers & Test Structures, mikromasch catalog," Estonia, 2008.

[38] M. Taub, M. B., K. G., and L. E., *SPM Training Manual*. Laboratory for Advanced Materials, Stanford University, 2 ed., July 2003.

[39] P. Markiewicz and M. C. Goh, "Simulation of atomic force microscope tip-sample/sample-tip reconstruction," *J. Vac. Sci. Technol.*, vol. 13, pp. 1115–1118, May 1995.

[40] J. N. Israelachvili.

[41] J. C. Kotz, P. M. Treichel, and G. C. Weaver, *Chemistry and Chemical Reactivity*, p. 568. Brooks Cole, 6th ed., 2005.

[42] Agilent Technologies, Inc., *Agilent Technologies 5500 Scanning Probe Microscope*, Sept. 2010.

[43] C. C. W. Y. Martin and H. K. Wickramasinghe, "Atomic force microscope-force mapping and profiling on a sub 100-å scale," *J. Appl. Phys.*, vol. 61, pp. 4723–4729, May 1987.

[44] Q. Zhong, D. Inniss, K. Kjoller, and V. Elings, "Fractured polymer/silica fiber surface studied by tapping mode atomic force microscopy," *Surface Science*, vol. 290, no. 1-2, pp. L688–L692, 1993.

[45] S. Yunxu, L. Danying, R. Yanfang, H. Dong, and M. Wanyun, "Three-dimensional structural changes in living hippocampal neurons imaged using magnetic ac mode atomic force microscopy," *J. Electron Microsc.*, vol. 55, no. 3, pp. 165–172, 2006.

[46] W. Han, S. M. Lindsay, and T. Jing, "A magnetically driven oscillating probe microscope for operation in liquids," *Applied Physics Letters*, vol. 69, no. 26, p. 4111, 1996.

[47] W. Han and S. M. Lindsay, "Probing molecular ordering at a liquid-solid interface with a magnetically oscillated atomic force microscope," *Applied Physics Letters*, vol. 72, no. 13, pp. 1656–1658, 1998.

[48] H.-J. Butt, B. Cappella, and M. Kappl, "Force measurements with the atomic force microscope: Technique, interpretation and applications," *Surface Science Reports*, vol. 59, no. 1-6, pp. 1–52, 2005.

[49] J. L. Hutter and J. Bechhoefer, "Calibration of atomic-force microscope tips," *Rev. Sci. Instrum.*, vol. 64, pp. 1868–1873, Jul. 1993.

[50] B. M. Gumbiner, "Cell Adhesion: The Molecular Basis of Tissue Architecture and Morphogenesis," *Cell*, vol. 84, no. 3, pp. 345–357, 1996.

[51] C. M. Franz, A. Taubenberger, P.-H. Puech, and D. J. Muller, "Studying Integrin-Mediated Cell Adhesion at the Single-Molecule Level Using AFM Force Spectroscopy," *Sci. STKE*, vol. 2007, no. 406, p. pl5, 2007.

[52] W. T. Johnson, G. Kada, C. Stroh, H. Gruber, H. Wang, F. Kienberger, A. Ebner, S. Lindsay, and P. Hinterdorfer, "Simultaneous Topography and RECognition Mapping with PicoTREC: A Powerful New Technology That Can Be Used To Map Nanometer-Scale Molecular Binding Sites On A Variety Of Surfaces," in *Technical Proceedings of the 2005 NSTI Nanotechnology Conference and Trade Show*, vol. 2, pp. 679–682, 2005.

[53] C. Stroh, H. Wang, R. Bash, B. Ashcroft, J. Nelson, H. Gruber, D. Lohr, S. M. Lindsay, and P. Hinterdorfer, "Single-molecule recognition imaging microscopy," *PNAS*, vol. 101, no. 34, pp. 12503–12507, 2004.

[54] "Nikon microscopyu - water immersion objectives." http://www.microscopyu.com/articles/optics/waterimmersionobjectives.html. [Online; accessed 27-June-2011].

[55] J. F. W. Herschel, "Light," in *Transactions Treatises on physical astronomy, light and sound contributed to the Encyclopaedia Metropolitana*, p. 491, Richard Griffin & Co., 1828.

[56] G. B. Airy, "On the Diffraction of an Object-glass with Circular Aperture," in *Transactions of the Cambridge Philosophical Society, Vol. 5*, pp. 283–291, 1835.

[57] N. S. Claxton, T. J. Fellers, and M. W. Davidson, *Microscopy, Confocal.* John Wiley & Sons, Inc., 2006.

[58] L. Rayleigh *Phil. Mag.*, vol. 8, no. 5, p. 261, 1879.

[59] L. Martin, *Theory of the Microscope.* New York: American Elsevier Pub. Co., 1966.

[60] A. Nolte, L. Höring, and M. W. Davidson, "Zeiss Education in Microscopy and Digital Imaging: Fundamentals of Illumination Sources for Optical Microscopy." http://zeiss-campus.magnet.fsu.edu/articles/lightsources/lightsourcefundamentals.html. [Online; accessed 13-June-2011].

[61] M. Minsky, "U.S. Patent No. 3013467 (A) - Microscopy apparatus."

[62] M. Kasha, "Characterization of electronic transitions in complex molecules," *Discuss. Faraday Soc.*, vol. 9, pp. 14–19, 1950.

[63] "Olympus Microscopy Resource Center — Confocal Microscopy - Fluorescence Excitation and Emission Fundamentals." http://www.olympusmicro.com/primer/techniques/confocal/fluoroexciteemit.html. [Online; accessed 21-April-2011].

[64] J. R. Lakowicz, *Introduction to Fluorescence.* Springer, Sep. 2006.

[65] T. Förster, "Zwischenmolekulare Energiewanderung und Fluoreszenz," *Annalen der Physik*, vol. 437, no. 1-2, pp. 55–75, 1948.

[66] D. Axelrod, D. Koppel, J. Schlessinger, E. Elson, and W. Webb, "Mobility measurement by analysis of fluorescence photobleaching recovery kinetics," *Biophysical Journal*, vol. 16, no. 9, pp. 1055–1069, 1976.

[67] A. Einstein, "On the Quantum theory of radiation," *Phys. Zeit.*, vol. 121, no. 18, pp. 63–77, 1917.

[68] J. F. Nye and M. V. Berry, "Dislocations in Wave Trains," *Proc. R. Soc. of London A: Mathematical and Physical Sciences*, vol. 336, no. 1605, pp. 165–190, 1974.

[69] "ZEISS Online Campus — Introduction to Superresolution Microscopy." `http://zeiss-campus.magnet.fsu.edu/articles/superresolution/introduction.html`. [Online; accessed 21-April-2011].

[70] T. A. Klar, S. Jakobs, M. Dyba, A. Egner, and S. W. Hell, "Fluorescence microscopy with diffraction resolution barrier broken by stimulated emission," *PNAS*, vol. 97, no. 15, pp. 8206–8210, 2000.

[71] K. I. Willig, B. Harke, M. Rebecca, and S. W. Hell, "STED microscopy with continuous wave beams," *Nat. Methods*, vol. 4, no. 11, pp. 915–918, 2007.

[72] S. W. Hell, "Toward fluorescence nanoscopy," *Nat. Biotechnol.*, vol. 21, pp. 1347–1355, Nov. 2003.

[73] S. W. Hell, "Strategy for far-field optical imaging and writing without diffraction limit," *Phys. Lett. A*, vol. 326, no. 1-2, pp. 140–145, 2004.

[74] S. B. Rodan and G. A. Rodan, "Integrin function in osteoclasts," *J. Endocrinol.*, vol. 154, pp. S47–S56, 1997.

[75] W. S. Group, "Prevention and management of osteoporosis," *WHO Technical Report Series*, vol. 921, 2003.

[76] R. P. Heaney, S. Abrams, B. Dawson-Hughes, A. Looker, A. Looker, R. Marcus, V. Matkovic, and C. Weaver, "Peak bone mass," *Osteoporosis International*, vol. 11, no. 12, pp. 985–1009, 2000.

[77] O. Filleul, E. Crompot, and S. Saussez, "Bisphosphonate-induced osteonecrosis of the jaw: a review of 2,400 patient cases," *J. Cancer. Res. Clin. Oncol.*, vol. 136, no. 8, pp. 1117–1124, 2010.

[78] M. R. McClung, E. M. Lewiecki, S. B. Cohen, M. A. Bolognese, G. C. Woodson, A. H. Moffett, M. Peacock, P. D. Miller, S. N. Lederman, C. H. Chesnut, D. Lain, A. J. Kivitz, D. L. Holloway, C. Zhang, M. C. Peterson, and P. J. Bekker, "Denosumab in Postmenopausal Women with Low Bone Mineral Density," *N. Engl. J. Med.*, vol. 354, no. 8, pp. 821–831, 2006.

[79] H. L. Judd, R. E. Cleary, W. T. Creasman, D. C. Figge, N. Kase, Z. Rosenwaks, and G. E. Tagatz, "Estrogen Replacement Therapy," *Obstetrics & Gynecology*, vol. 58, no. 3, 1981.

[80] J. A. Cauley, D. G. Seeley, K. Ensrud, B. Ettinger, D. Black, and S. R. Cummings, "Estrogen replacement therapy and fractures in older women," *Annals of Internal Medicine*, vol. 122, no. 1, pp. 9–16, 1995.

[81] W. C. Dougall, M. Glaccum, K. Charrier, K. Rohrbach, K. Brasel, T. De Smedt, E. Daro, J. Smith, M. E. Tometsko, C. R. Maliszewski, A. Armstrong, V. Shen, S. Bain, D. Cosman, D. Anderson, P. J. Morrissey, J. J. Peschon, and J. Schuh, "RANK is essential for osteoclast and lymph node development," *Genes & Development*, vol. 13, no. 18, pp. 2412–2424, 1999.

[82] K. Matsuzaki, N. Udagawa, N. Takahashi, K. Yamaguchi, H. Yasuda, N. Shima, T. Morinaga, Y. Toyama, Y. Yabe, K. Higashio, and T. Suda, "Osteoclast Differentiation Factor (ODF) Induces Osteoclast-like Cell Formation in Human Peripheral Blood Mononuclear Cell Cultures," *Biochemical and Biophysical Research Communications*, vol. 246, no. 1, pp. 199 – 204, 1998.

[83] D. J. Hadjidakis and I. I. Androulakis, "Bone Remodeling," *Ann. NY Acad. Sci.*, vol. 1092, no. 1, pp. 385–396, 2006.

[84] L. G. Raisz, "Pathogenesis of osteoporosis: concepts, conflicts, and prospects," *J. Clin. Invest.*, vol. 115, no. 12, pp. 3318–3325, 2005.

[85] M. A. Horton, *Adhesion Receptors as Therapeutic Targets*, pp. 223–245. CRC, 1st ed., 1995.

[86] J. C. Angus and C. C. Hayman, "Low-pressure, Metastable Growth of Diamond and "Diamondlike" Phases," *Science*, vol. 241, no. 4868, pp. 913–921, 1988.

[87] K. V. Volkov, V. V. Danilenko, and V. I. Elin, "Synthesis of diamond from the carbon in the detonation products of explosives," *Combustion, Explosion, and Shock Waves*, vol. 26, no. 3, pp. 366–368, 1990.

[88] C. K. Riener, C. M. Stroh, A. Ebner, C. Klampfl, A. A. Gall, C. Romanin, Y. L. Lyubchenko, P. Hinterdorfer, and H. J. Gruber, "Simple test system for single molecule recognition force microscopy," *Analytica Chimica Acta*, vol. 479, no. 1, pp. 59–75, 2003.

[89] Y. Lyubchenko, L. Shlyakhtenko, R. Harrington, P. Oden, and S. Lindsay, "Atomic force microscopy of long DNA: imaging in air and under water," *PNAS*, vol. 90, no. 6, pp. 2137–2140, 1993.

[90] N. Crampton, W. A. Bonass, J. Kirkham, and N. H. Thomson, "Studying silane mobility on hydrated mica using ambient AFM," *Ultramicroscopy*, vol. 106, no. 8-9, pp. 765–770, 2006.

[91] A. P. Demchenko, *Introduction to Fluorescence Sensing*, pp. 162–165. Springer, 2009.

[92] J. L. Pelley, A. S. Daar, and M. A. Saner, "State of Academic Knowledge on Toxicity and Biological Fate of Quantum Dots," *Toxicological Sciences*, vol. 112, no. 2, pp. 276–296, 2009.

[93] T. J. Collins, "ImageJ for microscopy," *BioTechniques*, vol. 43, pp. S25–S30, July 2007.

[94] T. P., R. U. E., and U. M., "A Pyramid Approach to Subpixel Registration Based on Intensity," *IEEE Transactions on Image Processing*, vol. 7, pp. 27–41, Jan. 1998.

[95] R. Kassies, K. O. Van Der Werf, A. Lenferink, C. N. Hunter, J. D. Olsen, V. Subramniam, and C. Otto, "Combined AFM and confocal fluorescence microscope for applications in bio-nanotechnology," *J. Microsc.*, vol. 217, no. 1, pp. 109–116, 2005.

[96] M. König, F. Koberling, D. Walters, J. Viani, R. Ros, and O. Schulz, *Technical Note: Combining Atomic Force Microscopy with Confocal Microscopy.* PicoQuant GmbH, 2009.

Appendix

Photographs

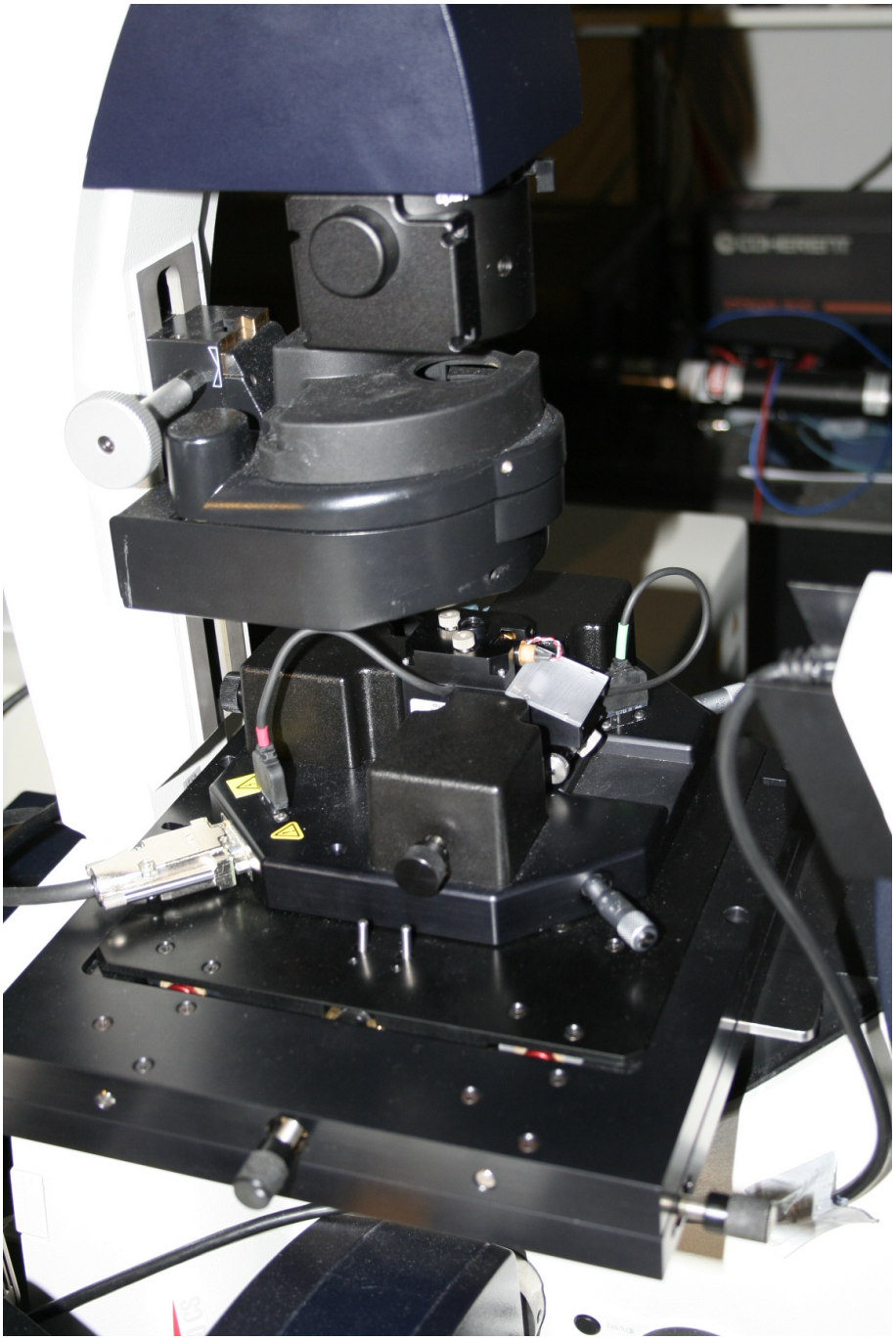

Figure 43. In this picture the AFM sample stage (originally designed for Zeiss invert microscopes) is installed to Leica microscope. Sample spot is controlled with micrometers which are seen in the picture.

Figure 44. Control units and computer to control AFM. The smaller black box is the MAC mode unit.

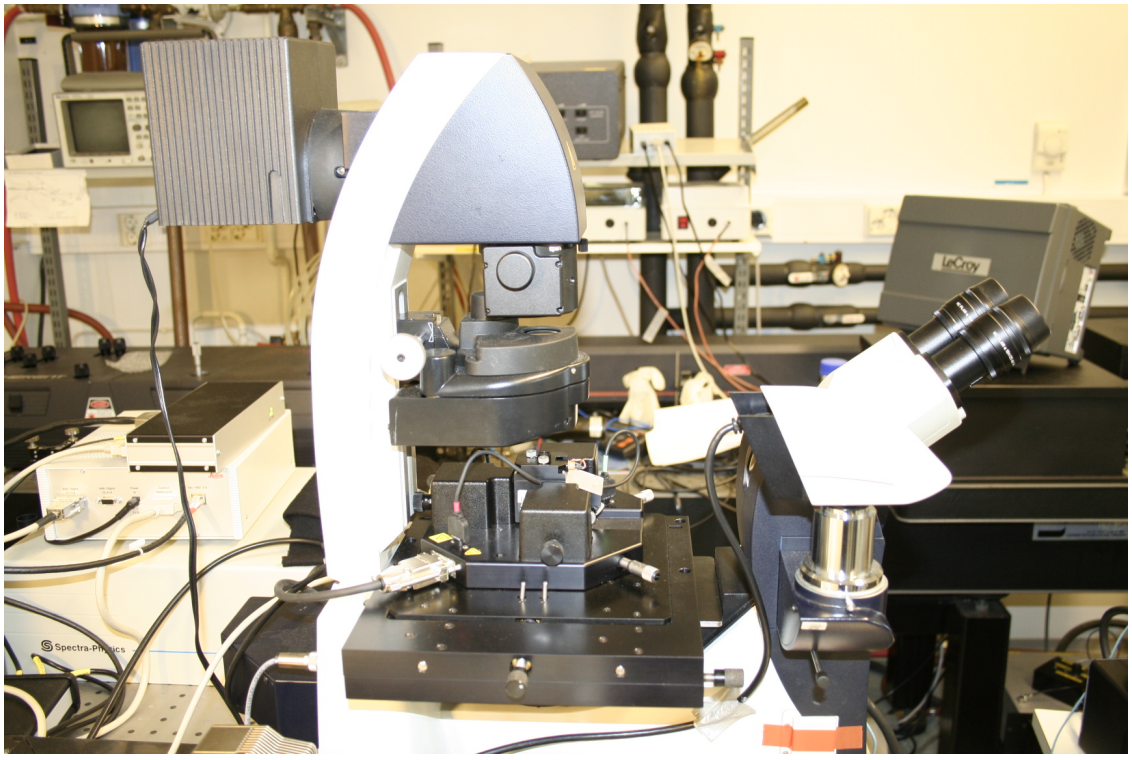

Figure 45. Side view of the installed setup.

Adapter pieces

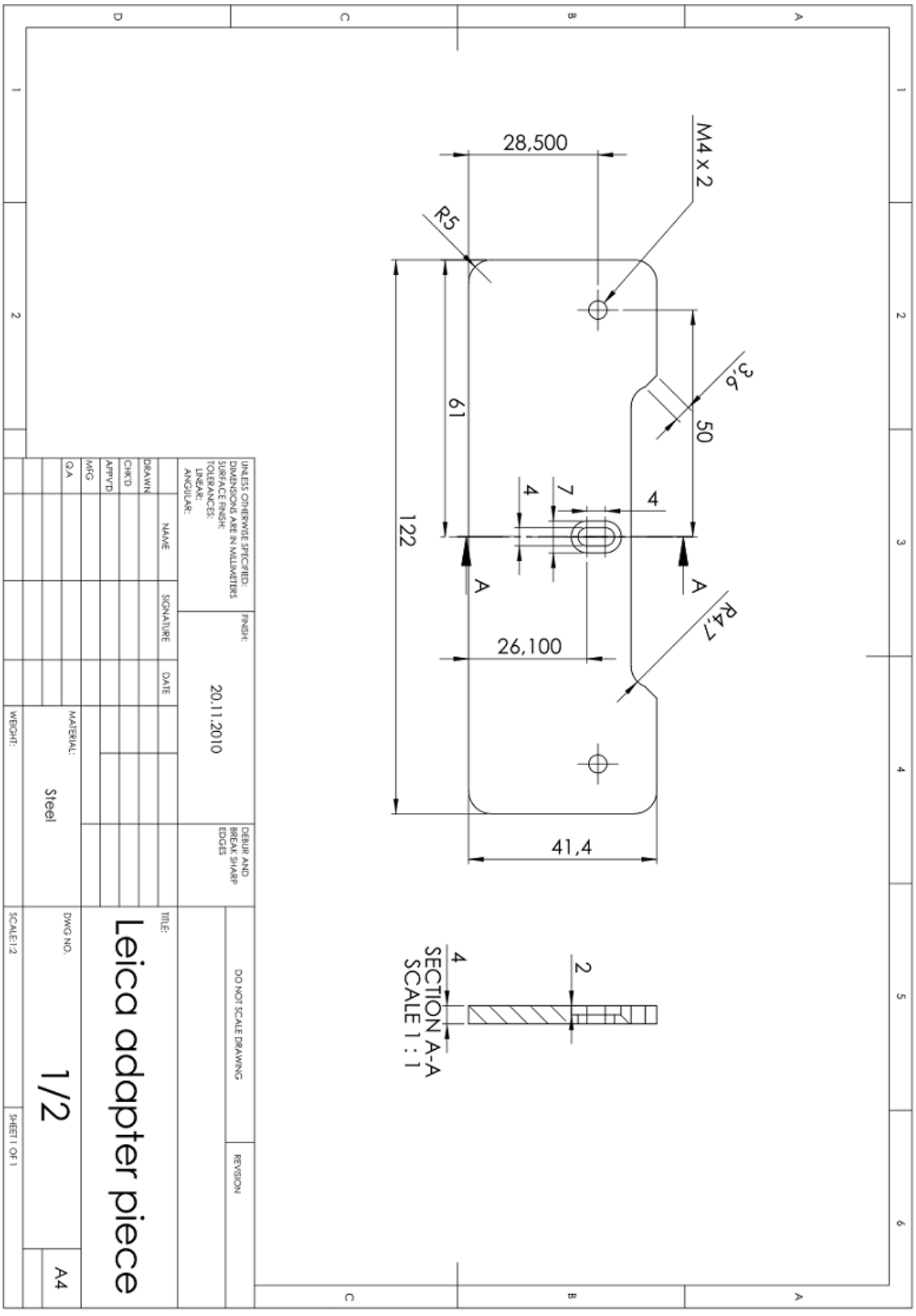

Figure 46. Front adapter piece for Quickslide stage. Drawing is made with AutoCAD2007 and all dimensions are in millimeters.

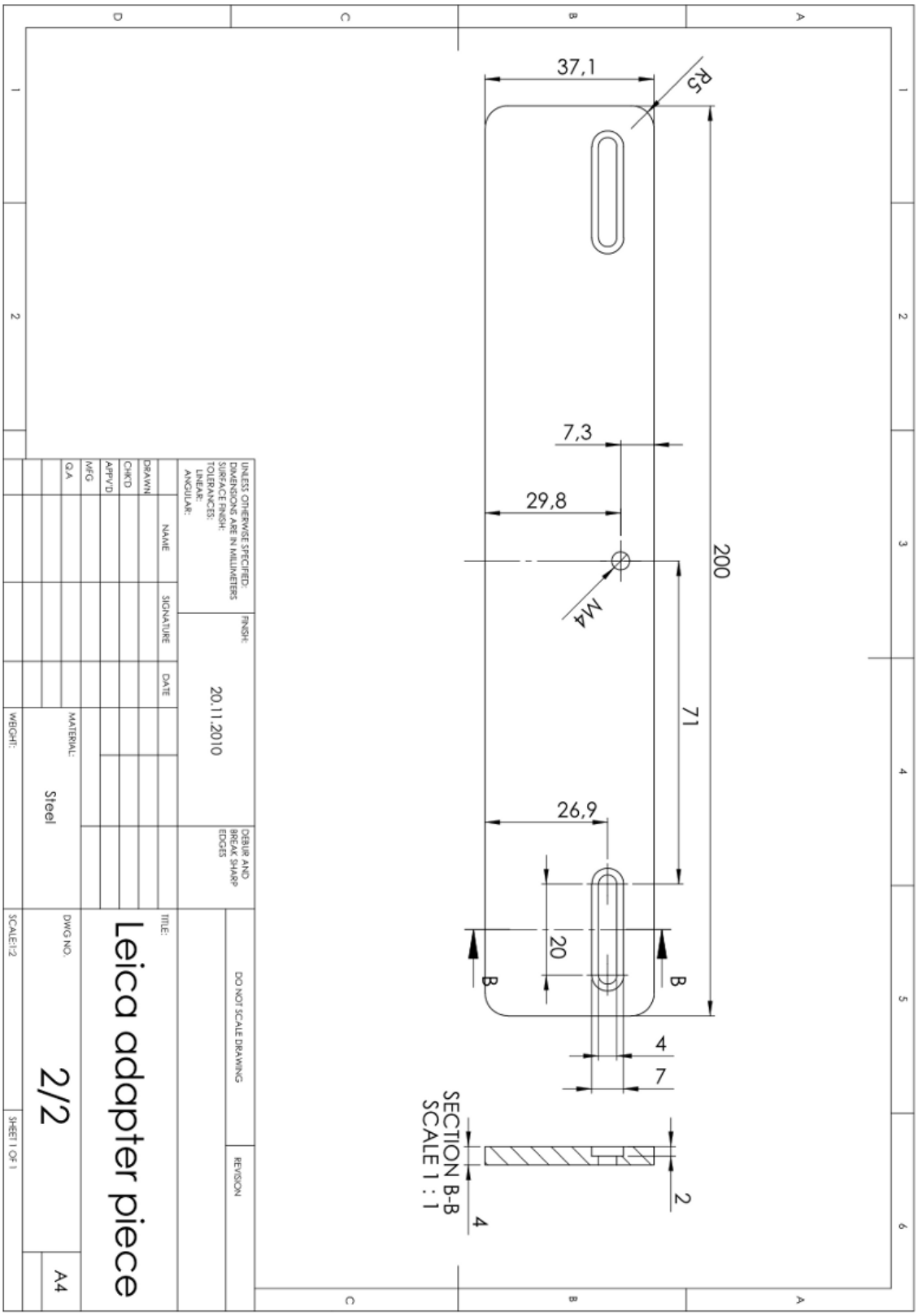

Figure 47. Back adapter piece for Quickslide stage. Drawing is made with AutoCAD2007 and all dimensions are in millimeters.